Mineralium Deposita (2024) 59:1–22
https://doi.org/10.1007/s00126-023-01194-8

ARTICLE

Timing and origin of skarn-, greisen-, and vein-hosted tin mineralization at Geyer, Erzgebirge (Germany)

Nicolas Meyer[1] · Gregor Markl[1] · Axel Gerdes[2,3] · Jens Gutzmer[4] · Mathias Burisch[4,5]

Received: 27 January 2023 / Accepted: 6 July 2023 / Published online: 1 August 2023

Abstract

This contribution presents new insights into the origin and age relationships of the Geyer tin deposit in the Erzgebirge, Germany. Tin mineralization occurs in skarns, greisen, and in cassiterite-bearing fluorite-quartz veins. Skarn alteration replaces marble layers of the Cambrian Jáchymov Group and occurs in two clearly distinct stages. The first skarn stage forms skarnoid textured assemblages of clinopyroxene, garnet, and wollastonite with no tin phases recognized. Garnet U-Pb ages of this skarn stage (~322 Ma) relate the earlier skarn stage to the emplacement of the Ehrenfriedersdorf granite (~324 to 317 Ma). The second stage of skarn alteration is marked by the occurrence of malayaite and cassiterite associated with garnet recording ages of 307 to 301 Ma. Greisen- and skarn-hosted cassiterite-bearing veins provide U-Pb ages in the range of 308 to 305 Ma, relating greisenization and vein formation to the same magmatic-hydrothermal event as the second skarn stage. This suggests that tin mineralization at Geyer is related to a distinctly younger magmatic-hydrothermal event, clearly postdating the Ehrenfriedersdorf granite, which was previously assumed as the source of the tin-rich fluids. Fluid inclusions show salinities in the range of 1.0 to 31.5 % eq. w($NaCl \pm CaCl_2$) and homogenization temperatures between 255 and 340 °C. Cassiterite-associated fluid inclusions show indications for heterogeneous entrapment and dilution of hydrothermal with meteoric fluids. Dilution of high-salinity fluids with low-salinity fluids and cooling of the system was probably a decisive process in the precipitation of cassiterite in the Geyer Sn system.

Keywords Magmatic-hydrothermal · LA-ICP-MS geochronology · Tin deposit · Garnet · Cassiterite

Introduction

The majority of global tin resources is hosted by various styles of magmatic-hydrothermal mineralization such as greisen, pegmatites, skarns, and veins related to highly evolved granitic systems (Breiter et al. 2017; Černý 1991; Chen et al. 1992; Jackson 1979; Lehmann 2021). In central Europe, tin systems are invariably related to late Paleozoic granites emplaced during the post-collisional stage of the Variscan orogeny (Förster et al. 1999). The Erzgebirge (Germany) is among Cornwall (UK), the Massif Central (France), the Iberian Massif (Spain/Portugal), and the Armorican Massif (France), one of Europe's prolific tin provinces (Lehmann 1990; Raimbault et al. 1995; Reinhardt et al. 2022; Romer and Kroner 2015, 2016). The Erzgebirge is host to polymetallic greisen-, skarn-, and vein-type deposits (Korges et al. 2020; Reinhardt et al. 2022; Swinkels et al. 2021), of which the known skarn deposits of the Erzgebirge, as a group, reflect the largest tin resource in Europe (Elsner 2014). In addition to Sn,

Editorial handling: B. Lehmann

✉ Nicolas Meyer
nicolas.meyer@uni-tuebingen.de

✉ Mathias Burisch
burisch@mines.edu

[1] Fachbereich Geowissenschaften, Petrologie und Mineralische Rohstoffe, Eberhard Karls Universität Tübingen, Tübingen, Germany

[2] Institut für Geowissenschaften, Goethe-Universität Frankfurt, Frankfurt, Germany

[3] Frankfurt Isotope and Element Research Center (FIERCE), Goethe-Universität Frankfurt, Frankfurt, Germany

[4] Institute Freiberg for Resource Technology, Helmholtz-Zentrum Dresden-Rossendorf, Freiberg, Germany

[5] Mineral System Analysis Group, Department of Geology and Geological Engineering, Colorado School of Mines, Golden, CO, USA

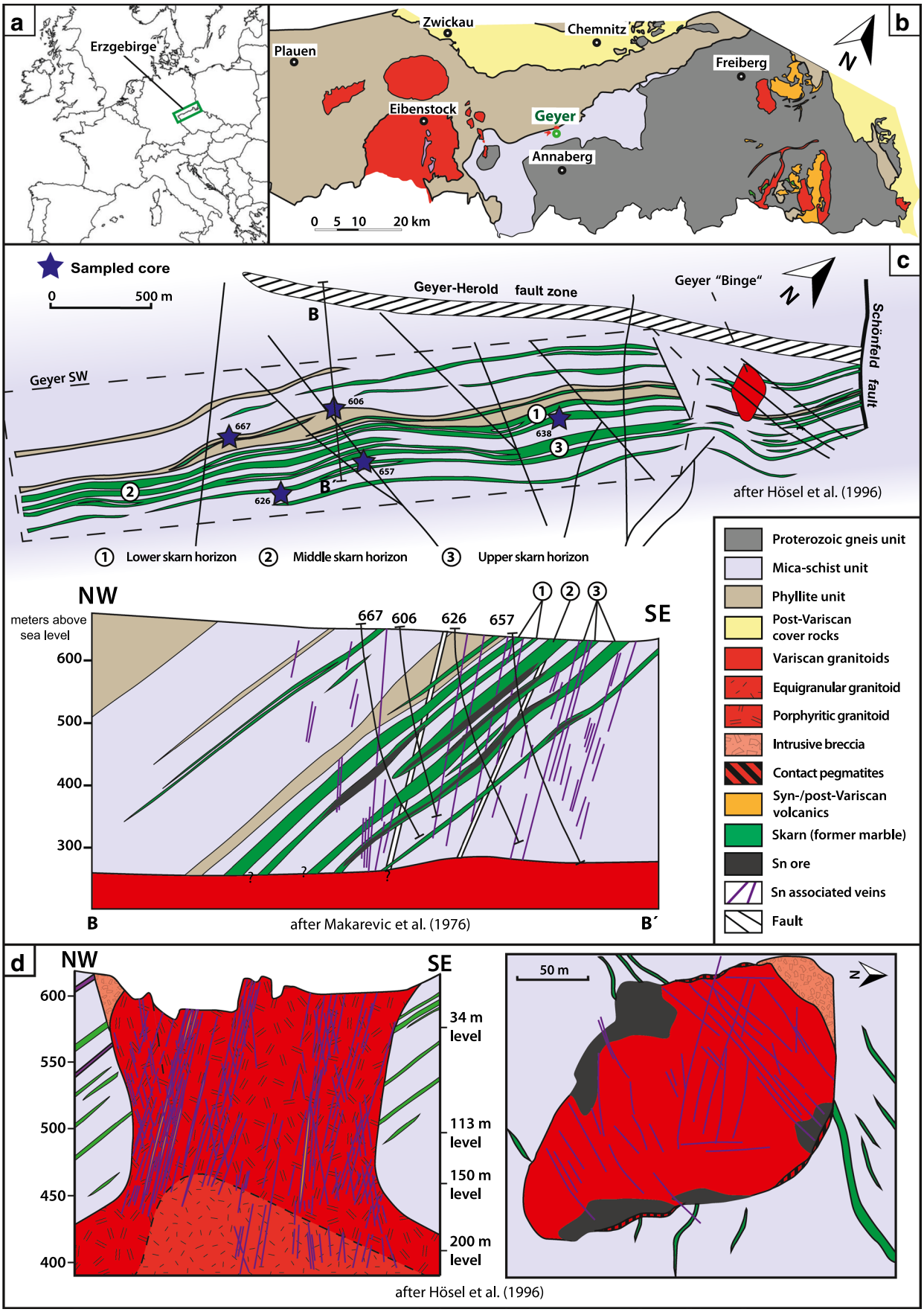
a
Erzgebirge
b
Zwickau
Chemnitz
Plauen
Freiberg
Eibenstock
Geyer
Annaberg
0 5 10 20 km
N
c
Sampled core
0 500 m
Geyer-Herold fault zone
Geyer "Binge"
Schönfeld fault
Geyer SW
B
B´
606
667
638
657
626
1
2
3
after Hösel et al. (1996)
① Lower skarn horizon ② Middle skarn horizon ③ Upper skarn horizon
NW
SE
meters above sea level
600
500
400
300
667 606 626 657
after Makarevic et al. (1976)
Proterozoic gneis unit
Mica-schist unit
Phyllite unit
Post-Variscan cover rocks
Variscan granitoids
Equigranular granitoid
Porphyritic granitoid
Intrusive breccia
Contact pegmatites
Syn-/post-Variscan volcanics
Skarn (former marble)
Sn ore
Sn associated veins
Fault
d
NW
SE
600
550
500
450
400
34 m level
113 m level
150 m level
200 m level
50 m
N
after Hösel et al. (1996)

◂**Fig. 1** **a** Geographic overview map. **b** Simplified geological overview map of the Erzgebirge including the location of the Geyer system. **c** Geological map and cross-section of the study area. The skarn layers are orientated parallel to the foliation of the surrounding low- to medium-grade meta-sedimentary units, trending NE-SW. Skarns are delimited by the Schönfeld fault in the northeast. The cross-section shows that the skarns are underlain by a large-volume intrusion at depth, which has a sub-horizontal contact. The Geyersberg granite intrusive stock crops out in the north-east of the district (after Hösel et al. 1996). Skarn layers extend down-dip from the surface to the top of the underlying pluton with a dip of about 45° NW. Veins and faults intersect the skarn lenses (after Makarevič et al. 1976). **d** Geological cross-section and overview map of the Geyersberg area including the historic pit of the Geyer "Binge"

some of the skarns in the Erzgebirge also host significant resources of W, Zn, Fe, and In—in addition to Sn (Bauer et al. 2019; Hösel 1994; Hösel 2002; Lorenz and Hoth 1967; Reinhardt et al. 2021).

Despite their economic significance, detailed geological descriptions and geochemical data are for many occurrences limited to technical reports and resource estimates related to the tin exploration program of the former German Democratic Republic (GDR; 1945–1989). Consequently, most of the skarn systems in the Erzgebirge have not been subject of studies with modern geochemical methods, with the exception of a few recent studies that focused on the Hämmerlein (Bauer et al. 2019; Kern et al. 2019; Korges et al. 2020; Lefebvre et al. 2019) and Waschleithe deposits (Reinhardt et al. 2021), both located in the Schwarzenberg district in the western part of the Erzgebirge (Schuppan and Hiller 2012).

The Geyer mining district (~5 × 4 km) is also located in the western part of the Erzgebirge, ~25 km south of Chemnitz. Historic tin (and minor tungsten and iron) mining occurred between 1395 and 1913 in the Geyer area. After World War II, an extensive exploration campaign was carried out by the SDAG Wismut targeting skarn-hosted tin mineralization in the area south-west of the outcropping Geyersberg stock. This resulted in 123 boreholes with more than 37,000 m of recovered core material (Hösel et al. 1996). In 2011 and 2012, Tin International drilled four new confirmation boreholes in the Geyer SW area, which were used to constrain an indicated resource of 46 kt of tin at an average ore grade of 0.56% Sn (Elsner 2014). Toward the northeast, the Geyer skarn- and greisen-hosted deposit is separated by the NW–SE trending Geyer-Schönfeld fault system from the stockwork-hosted Ehrenfriedersdorf tin deposit (Hösel 1994). Th-U-Pb dating of uraninite in granites from the nearby Ehrenfriedersdorf district (Greifensteine and Sauberg) and U-Pb dating of apatite from granite (Sauberg) provide intrusion ages between 324 ± 4 and 319.7± 3 Ma, 323.9 ± 3, and 317.3 ± 2 Ma, respectively (Romer et al. 2007), whereas no geochronological data is available for the intrusions at Geyer. The intrusion depth is constrained by melt inclusion analyses to 2.5–4 km (Breiter et al. 1999).

The origin and timing of skarn-hosted tin mineralization were controversially debated (Lefebvre et al. 2019) until direct geochronological data (U-Pb ages of garnet using LA-ICP-MS) revealed the magmatic-hydrothermal origin of skarn formation in the Erzgebirge. On the scale of the Erzgebirge, skarn-related garnet ages range from 335 to 295 Ma (Burisch et al. 2019; Reinhardt et al. 2022), which coincide with late-collisional magmatic (335–310 Ma) and post-orogenic volcanic rock units (305–285 Ma; Luthardt et al. 2018; Romer et al. 2007; von Seckendorff et al. 2004) in the region. Cassiterite is the main tin ore mineral. In the Hämmerlein deposit, the most important tin skarn resource of the Erzgebirge, cassiterite is usually associated with chlorite-actinolite-quartz alteration that replaces early-stage skarn or occurs also as infill of veinlets cross-cutting the skarn bodies and surrounding host rocks (Kern et al. 2019). Conversely, cassiterite in greisen is associated with typical greisen minerals such as mica, quartz, fluorite, and topaz, which may occur as discrete veins or disseminations (Hösel et al. 1996). In this study, we present field and petrographic observations, *in situ* U-Pb dating, and fluid inclusion microthermometric data to constrain the timing and underlying processes of greisen and skarn alteration and related ore formation at the Geyer SW deposit.

Regional geology and skarn-related fluids

The Erzgebirge-Krušné hory is a ~160 × 35 km exposure of mainly metamorphic rocks belonging to the Bohemian Massif within the Saxothuringian zone of the European Variscan Belt (Förster et al. 1999). The Erzgebirge comprises various metamorphic nappes (Rötzler 1995; Willner et al. 1997) that underwent peak metamorphic conditions at ~340 Ma (Kröner and Willner 1998). These units include gneisses, mica schists, marbles, phyllites, and metavolcanic rocks (Fig. 1). Ondrus et al. (2003) and Tichomirowa et al. (2012) showed that the protoliths of these rocks are greywackes, conglomerates, granodiorites (gneiss units) or volcanic rocks, and marine sediments (mica schist and phyllite unit). After rapid uplift to middle and upper crustal levels (Schmädicke et al. 1995), the metamorphic units were intruded by highly evolved, late-orogenic peraluminous granites (335–310 Ma; Förster et al. 1999) accompanied by the emplacement of late- and post-collisional lamprophyric and rhyolitic dykes and other (sub)volcanic rocks (330–275 Ma; Bolduan 1963a; Hoffmann et al. 2013; Luthardt et al. 2018). The emplacement depths of late-orogenic granitic batholiths and stocks in the western part of the Erzgebirge have been constrained to 3–6 km using melt inclusion analyses (Breiter et al. 1999; Thomas and Klemm 1997).

The Erzgebirge hosts numerous hydrothermal skarn, greisen, and vein-type deposits genetically related to late- and

post-collisional magmatism in the area (Burisch et al. 2019; Legler 1985; Swinkels et al. 2021; Tischendorf and Förster 1990; Zhang et al. 2017). U-Pb LA-ICP-MS data on cassiterite define a mineralization age of 326–320 Ma of the mineralization for the Ehrenfriedersdorf tin deposit (Zhang et al. 2017). These ages might be doubtful and are probably up to 8 Ma younger than reported (Zhang pers. comm.). Multimineral Rb-Sr geochronology on greisen and skarn samples from the Hämmerlein deposit indicates three age groups: ~340 Ma obtained from skarn associated white mica, K-feldspar, and fluorite, and ~320 Ma and 290 Ma from greisen-associated muscovite, apatite, and K-feldspar (Lefebvre et al. 2019). Re-Os dating of hydrothermal molybdenite from greisen of the Altenberg Sn-(W-Mo) complex reveals mineralization ages of 326–319 Ma (Romer et al. 2007). U-Pb LA-ICP-MS data of skarn-related garnet range from ~335–295 Ma (Burisch et al. 2019; Reinhardt et al. 2022) spanning a much broader range than greisen-related ages. Garnet ages related to skarns with significant metal endowment define at least two principal stages: an older group of skarns formed at ~325–313 Ma, which coincides with available greisen-related ages and late-collisional magmatism, whereas a younger skarn stage occurred at ~310–295 Ma, post-dating late-collisional intrusions, but coinciding with post-collisional volcanic activity (Burisch et al. 2019; Hoffmann et al. 2013; Löcse et al. 2023; Reinhardt et al. 2022).

Fluid inclusions in skarn-associated garnet and clinopyroxene from the Sn-Zn-In Hämmerlein deposit and from the Waschleithe Zn-skarn in the Schwarzenberg district show homogenization temperatures of 270–385 °C with salinities ranging from 0.3–3.8% eq. w(NaCl), while those in skarn-related fluorite has lower homogenization temperatures (210–225 °C), but higher salinities (~7.7% eq. w(NaCl); Korges et al. 2020; Reinhardt et al. 2021). Korges et al. (2020) recently reported fluid inclusions in skarn-hosted cassiterite from the Hämmerlein deposit with unusually high homogenization temperatures (500 °C) and high salinities (30–47% eq. w(NaCl)), whereas coexisting greisen-hosted fluid inclusions in cassiterite and quartz have lower formation temperatures (350–400 °C) and lower salinities (1.9–6.0% eq. w(NaCl); (Korges et al. 2020). Fluid inclusions in vein-hosted fluorite and greisen-hosted quartz have homogenization temperatures around 450 °C, with salinities of 11–14% eq. w(NaCl), and a second group has lower homogenization temperatures of 210 to 325 °C and salinities between 2.0 and 9.0% eq. w(NaCl) (Korges et al. 2020).

The Geyer district

The geological architecture of the Geyer district is dominated by SW-NE striking and NW dipping paragneisses, mica schists, and phyllites of the Cambrian Jáchymov Group, with intercalations of dolomitic to calcitic marbles and quartzites (Hösel 1994). This succession was metamorphosed at low- to medium-grade during the Variscan orogeny and later intruded by a composite intrusion present below the surface in the entire area (Bolduan 1963a; Hermann 1967; Hösel et al. 1996; Tischendorf et al. 1965; Tischendorf and Förster 1990). The contact between the granitoids and the metamorphic host rocks is almost horizontal (at a depth of ~150–450 m below surface level; see Fig. 1c), except for the stock-like Geyersberg intrusion, which forms a prominent outcrop in the eastern part of the district (Fig. 1d). The flanks of this intrusive stock dip almost vertically to a depth of 180 m, where they become significantly shallower (Fig. 1d). The Geyersberg composite stock consists mainly of two types of intrusions. An older granitic suite is with fine- to coarse-grained porphyritic texture and high biotite content (Bolduan 1963a). This older intrusion is not associated with significant greisen alteration nor Sn mineralization (Hösel et al. 1996). The younger main intrusive stage cross-cuts the older intrusion and is characterized as an equigranular, low-biotite topaz-bearing granite (Bolduan 1963a). This second intrusion contains up to 4 wt% fluorine and hosts abundant disseminated cassiterite and lithium-bearing mica (Bolduan 1963a, 1963b; Breiter et al. 1999; Hösel 1994; Hösel et al. 1996) and an intrusive breccia body. To greater depth (~450 m), the texture of the intrusive units merges into a fine-grained, porphyritic granite, which coincides with an increase of biotite and a decreasing topaz content (Hösel 1994). Rhyolitic dykes cross-cut the main intrusions (Bolduan 1963a; Hösel et al. 1996). "Stockscheider" pegmatites occur at the contact between the individual intrusions and at the contact with the surrounding metasedimentary units. Hornfels and mica schists with contact metamorphic biotite, cordierite, and andalusite are abundant in the contact aureole, which is developed to a distance of ~50 m away from the intrusive contact (Hösel et al. 1996).

Minor fluorite-quartz, fluorite-barite, native metal-arsenide, and Mn-Fe veins occur in the Geyer area (Bolduan 1963a). These mainly Mesozoic and Cenozoic veins are genetically unrelated to Sn mineralization (Burisch et al. 2021, 2022; Guilcher et al. 2021; Haschke et al. 2021; Kuschka 1994) and hence not discussed any further.

Geyer SW skarn

The majority of Sn mineralization at Geyer SW is hosted by exoskarns that mainly replaced marble but also mica schists in direct vicinity of the marble units (Fig. 1c). Most of the marble units intersected by exploration drill cores at Geyer SW are to some degree affected by skarn alteration, but there are a few drill cores (e.g., BZ 667/75

at 412.2-414.0 m) which intersect macroscopically unaltered marble. Three distinct skarn units (from NW to SE 1, 2, and 3; Fig. 1c) have been distinguished (Hösel et al. 1996) which are dipping to the NW with an angle of about 30–40°, parallel to the metamorphic layering. Each of these skarn units is composed of several skarn layers thought to represent former carbonate layers (Hösel et al. 1996) and forms laterally discontinuous lens-shaped ore bodies. The lower skarn unit contains two discrete skarn layers and can be traced over a strike length of 3 km and extends down to the granite surface at depth, without any recognition of endoskarn (Fig. 1c). The lower layer with a thickness of 5–20 m is composed of two individual skarn bodies and one ore body. The upper layer with a thickness of 15–40 m comprises several skarn bodies replacing marble and adjacent mica schists. Two discrete ore bodies have been recognized in the upper layer (see Fig. 1c). The middle skarn unit has a strike length of 1.5 km and pinches out at a depth of about ~180 m above the granite contact (Hösel et al. 1996). It is characterized by a constant thickness of about ~20 m and contains several individual skarn bodies (Fig. 1c). The lower part of the middle skarn unit hosts only one ore body.

The upper skarn unit can be traced over a lateral distance of more than 3 km. It extends down to the granite contact and contains two individual skarn layers. Similar to the lower skarn unit, no endoskarn is documented in association with this skarn unit. The lower layer (total thickness of 7–25 m) consists of three skarn bodies and one ore body with a thickness between 1 and 6 m, which are separated by unaltered mica schists. The upper layer is again separated from the other skarn layer by unaltered mica schists and has a constant thickness of 15–20 m with several laterally discontinuous lens-shaped skarn bodies and one discrete ore body in the lower part of this layer. Many smaller skarn bodies have been additionally identified in the district. These are typically of only minor thickness and do not host significant tin mineralization.

Skarn mineralogy at Geyer comprises clinopyroxene and garnet with minor wollastonite, epidote, vesuvianite, magnetite, and fluorite in highly variable modal abundances (Hösel et al. 1996). These mineral assemblages are overgrown or replaced by chlorite, actinolite, fluorite, and cassiterite as well as base metal sulfides. High grades of skarn-hosted disseminated cassiterite are intimately associated with magnetite-rich domains, which have been reported to be mainly present within a distance of 450–300 m distance to the granite contact (Hösel et al. 1996). The bulk of tin resources (~80%) is hosted by skarn affected by chlorite-actinolite alteration and by fluorite-quartz or fluorite-chlorite veins intersecting the skarns and metasedimentary units with a maximum thickness of 15 cm (Hösel et al. 1996).

Geyer Binge greisen

Most of the historic underground mining activity at Geyer focused on the "Binge," the exposed Geyersberg granite (Fig. 1c and d), which forms a stock-like intrusive body with a diameter of around 230 m (Hoth and Wolf 1986). Greisen alteration and associated cassiterite mineralization predominantly develop along NE-SW and NW-SE striking, steeply and flat dipping veins that form a dense stockwork within the granite. These vein swarms consist of individual veins, ranging in length from 2 to 6 m, having a variable alteration halo (Hösel et al. 1996). Mineralogically, the alteration halo and veins mainly comprise topaz, lithium mica, and cassiterite (Bolduan 1963a). Most cassiterite is hosted by hydrothermal veins and related greisen alteration. Molybdenite and wolframite may also be recognized in some of these veins, but clearly predate cassiterite based on petrographic observations. A variety of hydrothermal veins cross-cut greisen alteration and cassiterite veins. They may comprise quartz, fluorite, hematite, and minor barite. They typically occur in different orientation or as the latest vein infill and are genetically unrelated, based on their mineralogy and cross-cutting relationships (Hösel 1994).

Sampling and methodology

A total of 60 samples from the Geyer mining district were collected from six drill cores from the Wismut SDAG and Tin International exploration campaigns. Access to drill cores was provided by the Geological Survey of the Free State of Saxony (LfULG). The sampling focused mainly on skarn bodies — both with and without significant tin mineralization — but also include some marble and mica-schist samples. 84 polished sections for petrographic investigations and 21 doubly polished sections for fluid inclusion analyses were prepared at the Helmholtz Institute for Resource Technology. Additionally, six garnet-rich samples and three cassiterite-rich samples were prepared as 1-inch epoxy rounds for LA-ICP-MS geochronology.

Petrography

Identification of minerals and examination of the textures were performed in transmitted and reflected light with a Leica DM750P light microscope and recorded with an Olympus single-lens reflex camera. This work was supported by scanning electron microscopy (SEM) performed on a Phenom XL SEM equipped with an energy dispersive X-ray spectrometer at the Geo- and Environmental Research Center (GUZ) of the University of Tübingen. Backscattered electron (BSE) images and qualitative mineral compositions were obtained with the SEM using a beam current of 15

nA and 15 kV acceleration voltage. Furthermore, cm-scale element maps were obtained by a microbeam XRF at the GUZ using a Bruker Tornado desktop unit equipped with a rhodium tube operating with 50 kV and 500 nA and two spectrometers. Element distribution maps were compiled using a 20 µm spot size on a 20 µm grid with dwell times of 10-16 milliseconds per pixel.

Fluid inclusion petrography and microthermometry

The fluid inclusion microthermometric measurements were carried out using a Leica light microscope equipped with a Linkam THMS 600 heating-freezing stage and a FLIR grasshopper3 USB camera at the GUZ Tübingen on doubly polished thick sections with a thickness of 150 µm. The classification of fluid inclusions into primary, secondary, and pseudosecondary inclusions follows the description of Roedder (1984). The stage was calibrated before and after each measurement campaign using synthetic fluid inclusion standards for the following phase transitions: melting temperature of ice (Tm_{ice}) and homogenization temperature (T_h) of pure H_2O and melting temperature of CO_2 (Tm_{CO2}) of H_2O-CO_2-standards. Tm_{ice} was used to calculate the salinity in the NaCl-H_2O system according to Steele-MacInnis et al. (2012). Melting temperature of halite (Tm_h), hydrohalite (Tm_{hh}), and Tm_{ice} were used to calculate salinities in the NaCl-$CaCl_2$-H_2O system after the spreadsheet of Steele-MacInnis et al. (2011). According to the classification criteria of Roedder (1984), fluid inclusions were classified as either primary, pseudosecondary, or clusters. Fluid inclusions with indications of metastability, post-entrapment modification, or leakage due to (micro)-fractures are excluded.

U-Pb LA-ICP-MS geochronology

Six samples with abundant garnet from the Geyer skarns and 3 cassiterite samples from greisen alteration and veins were selected for geochronology. The samples are from three drill cores and the scientific collection of Freiberg (Table 1). These samples cover textures and colors of skarn hosted garnet recognized in the exploration cores from Geyer SW; the garnets range from isometric, green garnet to anhedral garnet of red to beige color (Table 1 and ESM 1 and 2; Fig. 2). Samples selected for garnet U-Pb LA-ICP-MS geochronology exhibit a variable degree of retrograde overprint, with variable abundances of amphibole, chlorite, and fluorite. For U-Pb isotope analyses, samples with the lowest possible retrograde alteration and domains unaffected by retrograde overprint were selected to set the spots for LA-ICP-MS analysis. Cassiterite samples from veins contain fluorite and quartz; cassiterite from greisen samples is intergrown with quartz, sericite, and minor topaz. None of these samples exhibit hydrothermal overprint. Cassiterite crystals are euhedral and have a size up to 3 mm. In total, six skarn samples with abundant garnet and three cassiterite samples were cut to size and mounted in 1-inch epoxy rounds.

Uranium-Pb data were subsequently collected on a Thermo Scientific Element XR sector field ICP-MS coupled to a RESOlution (COMpex Pro 102) 193 nm ArF excimer laser equipped with a two-volume (Laurin Technic S155) ablation cell at the Frankfurt Isotope and Element Research Center (FIERCE), Goethe University Frankfurt (Germany) following the methodology of Burisch et al. (2019, 2022), Millonig et al. (2020), and Reinhardt et al. (2022). Measurement points for each polished section derive from a small area (<1 cm^2) and were set after careful screening before each analytical session to identify growth-zones with higher $^{238}U/^{206}Pb$ ratios and to avoid superficial exposure of mineral inclusions by monitoring trace element ratios during screening. Samples were then analyzed *in situ* in fully automated mode. During the measurements, the signals of ^{206}Pb, ^{207}Pb, ^{208}Pb, ^{232}Th, and ^{238}U were acquired by peak jumping in pulse counting mode with a total integration time of ~0.1 s, resulting in 360 mass scans. The raw data was corrected offline deploying an in-house Microsoft Excel spreadsheet program (Gerdes and Zeh 2006, 2009). Common Pb correction has not been applied to the data. Instead, U-Pb ages are calculated using linear regression in Tera-Wasserburg Concordia diagrams (Tera and Wasserburg 1972) since the ablated andradite-grossular and cassiterite incorporates a mixture of non-radiogenic and radiogenic Pb formed due to *in situ* decay of uranium. U-Pb dates are defined as the lower intercept of the regression line with the Concordia curve. Mali grandite (dated by ID-TIMS at 202.0 ± 1.2 Ma; Seman et al. 2017) and Swaziland cassiterite (3086 ± 3 Ma) were used as a primary reference material (RM), respectively. The age of Swaziland cassiterite was determined prior to this study using an approach similar to that described by Neymark et al. (2018). The $^{207}Pb/^{206}Pb$ ratio of multiple spot analyses on a single Swaziland cassiterite grain (1 × 0.6 cm) was NIST SRM612-mass bias corrected and yielded a weighted mean Pb/Pb age of 3086 ± 3 Ma. Excess of scatter on $^{207}Pb/^{206}Pb$ of NIST 612 (n = 20) for each session was around 0.14% (1 σ) and the mass bias varied from 0.7 to 0.4% between the different analytical sessions. Swaziland cassiterite typically yielded homogenous $^{206}Pb/^{238}U$ (e.g., 0.6141 ± 0.54%, 2 σ; n = 20) suggesting no disturbance of the U-Pb system. Therefore, the correction factor for $^{206}Pb/^{238}U$ was calculated using the percentage difference between the uncorrected $^{206}Pb/^{238}U$ age and the mass bias corrected $^{207}Pb/^{206}Pb$ of the Swaziland cassiterite. To verify the obtained $^{206}Pb/^{238}U$ fractionation correction, cassiterite from Pitkäranta (Neymark et al. 2018; Tapster and Bright 2020) and Ehrenfriedersdorf (inhouse RM) was measured as secondary quality control RM. Both RM yielded precise

Table 1 Description of samples and concentrations of U, Pb, and LA-ICP-MS U-Pb ages of garnet and cassiterite of the Geyer system

Sample number	Location	Description	U-Pb age (Ma)	MSWD	Initial $^{207}Pb/^{206}Pb$	U (µg/g)	Pb (µg/g)	*N*
GR1	Skarn SW Z626-96.5m	Green grt[1] with chl veins	301.6 ± 4.4 / 5.0	2.02	0.868	0.04–0.65	0.02–0.86	33
GR2	Skarn SW Z626-59m	Green grt[1] with pale green cpx	305.1 ± 3.0 / 3.9	1.22	0.880	0.01–0.36	0.01–0.09	25
GR4	Z626 85m	Pale red grt[1] with cpx and wo	322.4 ± 4.4 / 5.1	1.64	0.870	0.04–0.65	0.01–0.14	31
GR5	Z606 79.5m	Red grt[1] with red ves, wol	322.1 ± 10.7 / 11.8	11.38	0.865	0.01–1.8	0.05–0.39	27
GR6	Z626-45.6m	Pale green grt[1] with white cpx	307.3 ± 4.1 / 4.8	0.78	0.868	0.01–1.4	0.02–0.40	28
GR657	Z657-83.8m	cst[1] in fl-qz-vein	308.2 ± 1.9 / 3.7	0.81	0.868	1.4–16.5	0.08–1.2	35
60974	"Binge" Geyer	cst[1] with tpz and qtz in granite	305.7 ± 1.8 / 3.7	0.59	0.788	0.09–33.1	0.06–1.5	27
60973	"Binge" Geyer	cst[1] with tpz and qtz in granite	306.6 ± 1.5 / 3.5	0.84	0.788	1.4–14.2	1.4–14.1	33

[1]Analysed mineral; *MSWD*, mean square of weighted deviates; *N*, number of spot analyses; *grt*, garnet; *cpx*, clinopyroxene; *wo*, wollastonite; *ves*, vesuvianite; *chl*, chlorite; *cst*, cassiterite; *fl*, fluorite; *qz*, quartz; *tpz*, topaz

and reproducible (<1%) lower intercept ages during different analytical sessions (e.g., 1538.4 ± 6.7 and 1534.1 ± 6.4 Ma; 313.8 ± 2.1 and 314.1 ± 1.5 Ma, respectively). The perfect agreement of the Pitkäranta age with published ID-TIMS ages (1536.6 ± 1.0 Ma; Tapster and Bright 2020) also implies an accuracy of the applied method of better than 1%. Garnet RM Lake Jaco (dated by ID-TIMS by Seman et al. 2017), MaliGUF, and Ehrenfriedersdorf cassiterite (in-house reference materials) were employed as secondary quality control RM for garnet analyses. Primary and secondary RM were measured in duplicate after every 50 analyses of unknowns. All uncertainties are quoted at 2σ absolute and are quadratic additions of the within-run precision, counting statistics, background, excess of scatter (primary RM, NIST SRM-612), and excess of variance (Mali garnet and Swaziland cassiterite, respectively). Systematic uncertainties are reported as an expanded uncertainty, considering long-term reproducibility (0.8 %, 2σ) and decay constant uncertainties. A detailed description and location of drill core samples are summarized in ESM Table 2.

Results

In the following, mineralogical and petrographic investigations of host rocks, skarns, greisen alteration, and vein mineralization are presented. Macroscopic and microscopic observations (Figs. 3–6) were complemented by careful fluid

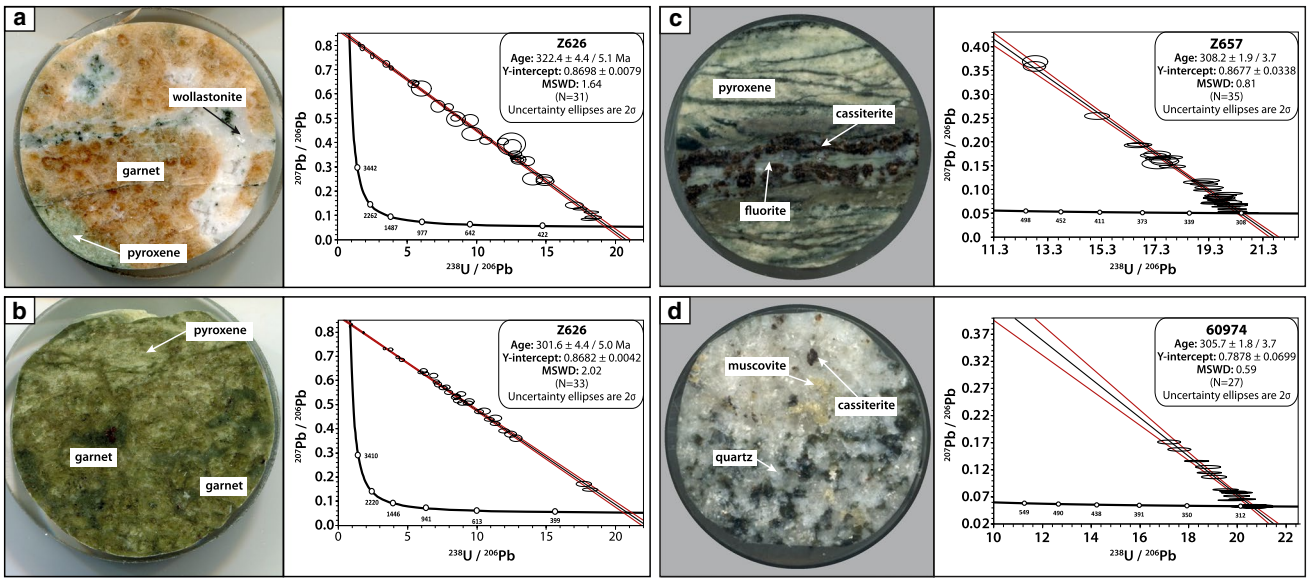

Fig. 2 Representative scans of age dated garnet and cassiterite with corresponding Tera-Wasserburg Concordia diagrams. Lower intercept ages are reported with internal/external uncertainties. **a** Pale red garnet of stage I with white wollastonite, **b** green garnet of stage II and clinopyroxene, **c** cassiterite-fluorite vein with chloritized alteration halo, and **d** greisenized granite with disseminated cassiterite

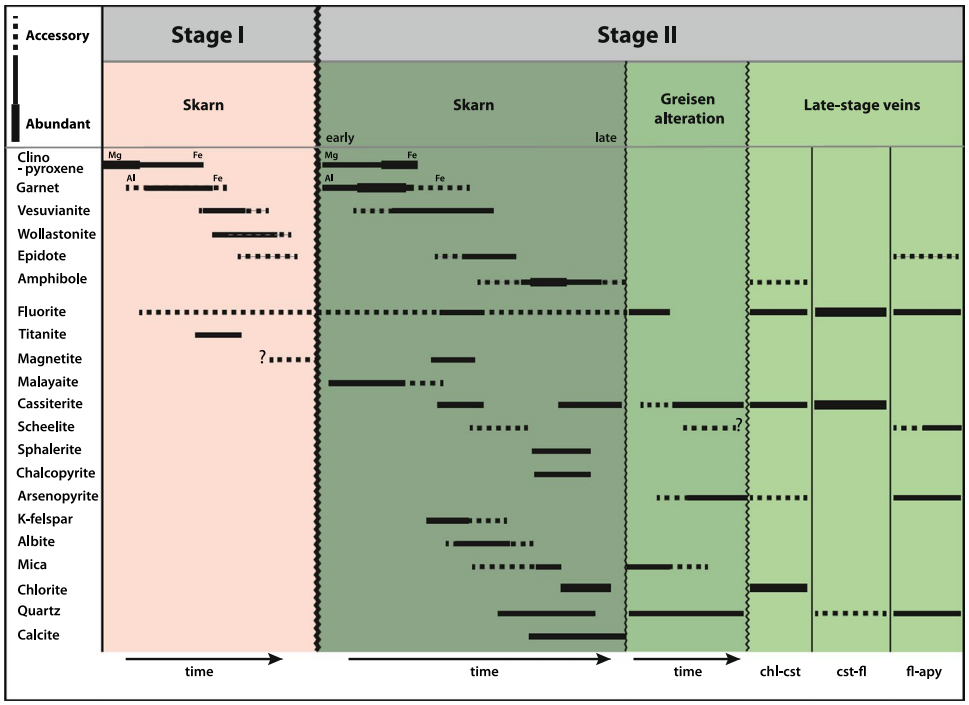

Fig. 3 Paragenetic sequence of skarn, greisen, and vein mineralization at Geyer, subdivided into two stages: stage I includes skarn stage I and stage II includes skarn stage II, greisen, and late-stage veins. Greisen and skarn alteration have the same paragenetic position but reflect spatial mineralogical variations that are controlled by protolith composition. Qualitative major element compositions of clinopyroxene and in garnet are indicated above the black bars

inclusion petrography (Fig. 7) and microthermometric analyses (Table 2). The complete background data set is provided in ESM Table 1. A selection of LA-ICP-MS U-Pb data are plotted in the Tera-Wasserburg diagram (Fig. 2), and a summary of geochronological data is provided in Table 1. LA-ICP-MS U-Pb background data is provided in ESM Table 2.

Host rock units

Mica schists

Mica schists are the most abundant rock unit in the Geyer area, containing biotite, muscovite, feldspar, garnet, rutile, and quartz as main components (Fig. 4a). On the m-scale, the mica schist composition is heterogeneous including garnet-bearing, graphite-bearing, and feldspar-rich layers (Fig. 5a). Apatite occurs locally as an accessory phase. Subordinate clinozoisite with an allanite component, zircon, but also sulfides like rammelsbergite, pyrite, and chalcopyrite may rarely occur. Mica shists can be overprinted by skarn alteration to some extent, with a gradual transition between both. These areas are characterized by a change toward green color due to the formation of clinopyroxene and chlorite.

Marble

Unaltered marble was only intersected in drill core BZ 667/75 at 412.2–414.0 m and is predominantly composed of anhedral calcite with an equigranular texture (Fig. 5b). Calcite crystals exhibit a size between 0.5 and 3.0 mm. Minor quartz (<0.2 mm), muscovite (<0.4 mm), and apatite (0.1–0.3 mm) occur as disseminations or as discrete bands, resulting in a weak metamorphic fabric. Furthermore, euhedral green metamorphic amphibole of (<2.0 mm) is recognized. This amphibole is distinctly different from skarn-related amphibole as it shows deformation features aligned with the metamorphic fabric of the surrounding mica schist. Thin veinlets are filled with chlorite, amphibole, or epidote together with chalcopyrite and sphalerite locally cross-cut the marble. In addition, progressive silicification of the marble is recognized close to the contact to the adjacent skarn.

Skarns

Mineral abundances and textures vary strongly across and within individual skarn bodies. Nevertheless, there are general similarities with respect to their petrographic and mineralogical composition, replacement textures, and cross-cutting relationships, which are summarized in a simplified paragenetic sequence (Fig. 3). Two types of skarn alteration can be distinguished based on their cross-cutting relationships, textures, and mineralogy: an early, pyroxene-dominated stage I skarn with fine-grained and Mg-richer minerals (Fig. 4a–c) is characterized by the preservation of the metamorphic fabric of the altered mica schist. Such texture is commonly referred to as a skarnoid skarn according to the terminology of Meinert et al. (2005). In the skarn I assemblages, no distinct tin phases or base metal sulfides are present. Younger garnet-pyroxene stage II skarn (Fig. 4d) is characterized by replacement textures that form euhedral minerals (Fig. 4d–f), which is consistent with metasomatic

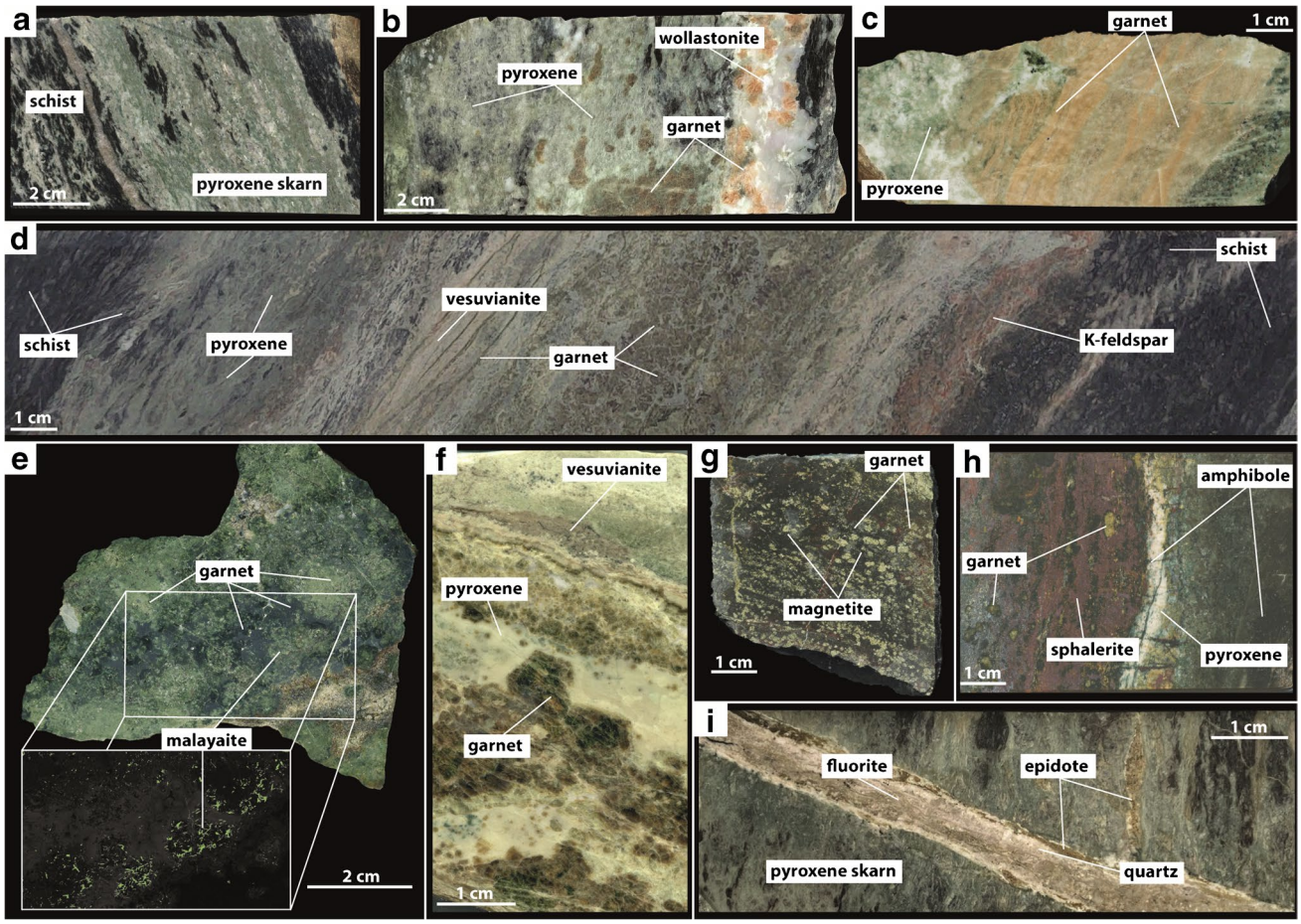

Fig. 4 Representative drill core intersections from Geyer. **a** Fine-grained pyroxene-dominated skarn of stage I skarn with mica-schist remnants (GM 10/60; 22.0–22.1 m). **b** Stage I skarn consisting of mainly anhedral clinopyroxene and garnet with some domains that contain euhedral garnet and wollastonite (BZ 667/75; 394.0–394.1 m). **c** Anhedral, very fine-grained red garnet intergrown with anhedral clinopyroxene of stage I skarn (BZ667/75; 190.6–190.7 m). **d** Complete intersection of a skarn lens with a fine-grained rim and isometric coarser-grained minerals in the center (Z626; 96.5–96.8 m). **e** Isometric skarn stage II with green garnet. The inlet shows the distribution of malayaite intergrown with garnet (GM 10/60; 29.8–30.2 m). **f** Coarse-grained euhedral garnet cogenetic with white clinopyroxene and a vesuvianite-rich domain of stage II skarn (Z626; 45.6–46.7 m). **g** Magnetite-rich skarn II with remnants of garnet (Z638; 80.2–80.3 m). **h** Amphibole and sphalerite-rich domains in skarn stage II with remnants of garnet and clinopyroxene (Y617; 116.4–116.8 m). **i** Fluorite-quartz-vein bordered by epidote cross-cutting a skarn layer (BZ667/75; 391.9–392.2 m)

skarn textures described by Meinert et al. (2005). Stage II skarn alteration is subdivided into (a) an early stage with garnet, clinopyroxene, vesuvianite, epidote, and other calc-silicate minerals (i.e., the prograde skarn evolution of Meinert et al. 2005) and (b) a late stage with amphibole, chlorite, and sulfide minerals (Fig. 4g and h) which would correspond to the retrograde skarn stage (Meinert et al. 2005). Since the euhedral vesuvianite is paragenetically coeval with garnet, it is ascribed to the early stage of skarn II formation.

Individual skarn layers typically exhibit a distinct geometry and may reach up to a few meters in thickness, but mostly do not exceed several tens of centimeters. Stage I skarn shows gradual transitions into the mica schists and often has irregularly-shaped patchy domains of unreplaced protolith (Fig. 4a). There seems to be no retrograde overprint associated with skarn stage I. Stage II skarn invariably occupies a central position of the individual skarn layers having thicknesses of 10 to 50 cm. Stage II skarn clearly replaces and postdates stage I skarn and even occurs as infill of fractures in skarn I. In contrast to skarn stage I, remnants of mica schist are rarely preserved in stage II skarns and the transition between skarn and metasedimentary rock is sharply defined. Vesuvianite-rich domains occur within garnet-skarn of both stages. Malayaite is the only distinct tin phase in the early phase of the second skarn alteration (cassiterite occurs later in the paragenetic sequence).

Lens-shaped domains and fractures filled with garnet, epidote, and vesuvianite, which have crystal sizes between tens of µm up to 3 cm, postdating the isometric stage II and the fine-crystalline stage I skarns, are interpreted as

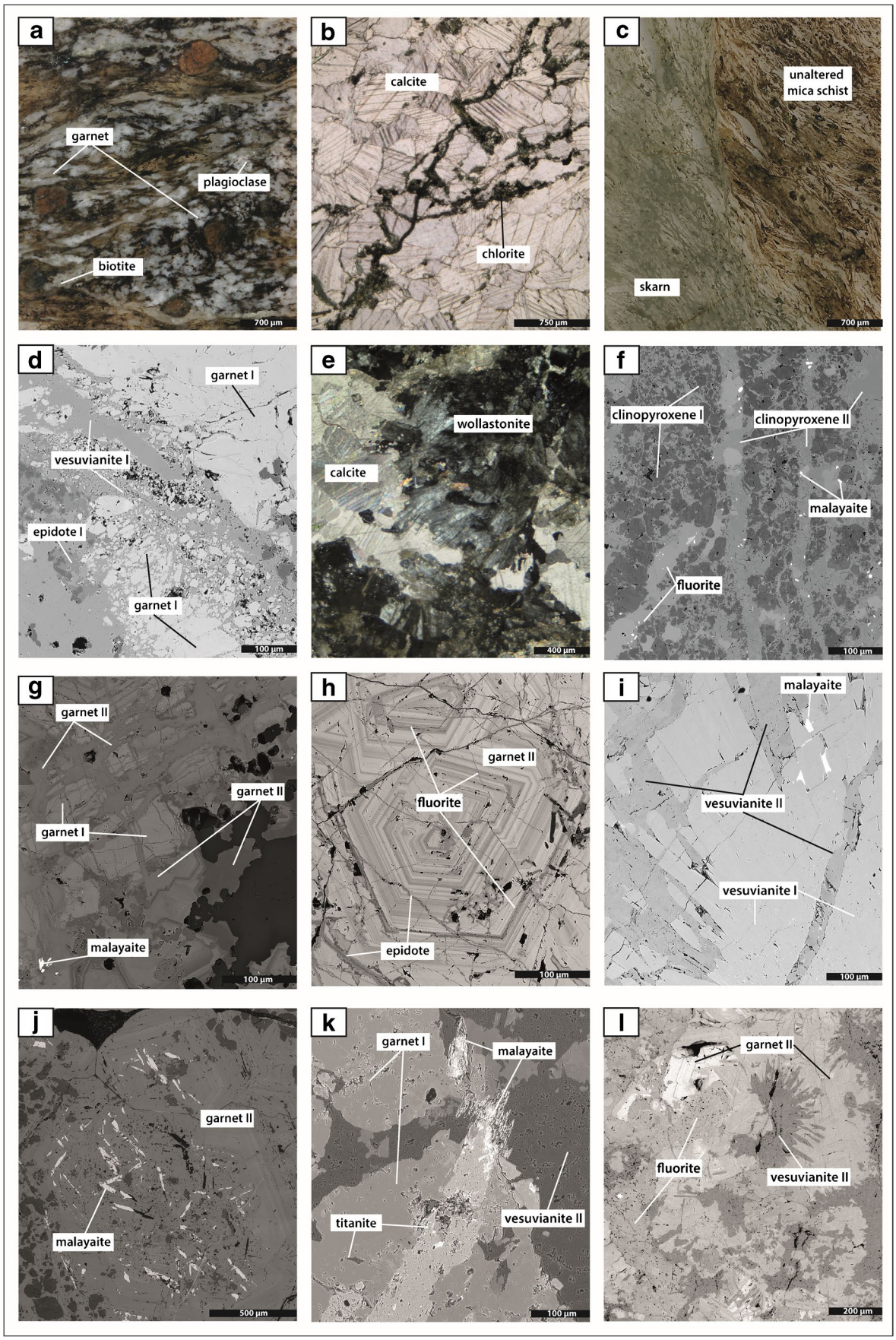
a
garnet
plagioclase
biotite
700 µm
b
calcite
chlorite
750 µm
c
unaltered
mica schist
skarn
700 µm
d
garnet I
vesuvianite I
epidote I
garnet I
100 µm
e
wollastonite
calcite
400 µm
f
clinopyroxene I
clinopyroxene II
malayaite
fluorite
100 µm
g
garnet II
garnet II
garnet I
malayaite
100 µm
h
garnet II
fluorite
epidote
100 µm
i
malayaite
vesuvianite II
vesuvianite I
100 µm
j
garnet II
malayaite
500 µm
k
garnet I
malayaite
titanite
vesuvianite II
100 µm
l
garnet II
fluorite
vesuvianite II
200 µm

◂**Fig. 5** Photomicrographs and backscattered electron microscopy images of characteristic minerals and textures of skarn and host rock. **a** Metamorphic texture of the metasedimentary host rock including mainly garnet, biotite, and quartz (GR-626-03b). **b** Subhedral calcite intersected by chlorite-filled veinlets (GR-667-11-03). **c** Contact between biotite schist and pyroxene skarn (GM-1-07B). **d** Garnet intersected by veins with vesuvianite and epidote infill (GR-667-10-02). **e** Grayish wollastonite replacing calcitic marble (GR-667-10-02). **f** Stage II clinopyroxene, malayaite, and fluorite replace clinopyroxene of skarn stage I (GR-626-06b). **g** Iron-rich garnet of skarn stage I is cross-cut by garnet with malayaite inclusions of skarn stage II (GR-626-04c). **h** Euhedral and zoned garnet of skarn stage II. Some of the growth zones are intergrown with coeval fluorite (GR-626-08a). **i** Vesuvianite of the first skarn stage, replaced, and cross-cut by vesuvianite II, which comprises malayaite inclusions (GR-667-16-03a). **j** Lath-shaped, euhedral malayaite enclosed by stage II garnet (GM-1-08c). **k** Lath-shaped titanite enclosed by garnet of skarn stage I. Both, titanite and garnet I, are intersected by vesuvianite; where titanite is in contact with vesuvianite it is replaced by malayaite (GR-667-1-01b). **l** Cogenetic garnet and vesuvianite of stage II replaced by fluorite (GR-626-04b)

transitional to later retrograde skarn textures and cassiterite-bearing veins. This late-stage alteration overprints both skarn stages and is characterized by the replacement of skarn minerals by amphibole, chlorite, quartz, and calcite. The alteration commonly centers on veinlets that cross-cut the skarn alteration; locally, the prograde skarn texture is almost completely replaced and only relicts are preserved. The thickness of these veinlets commonly does not exceed 5 cm, and their alteration halo shows minor chloritization of the adjacent host rock. These veins are mostly confined to skarns and can be traced only a few centimeters into the metasedimentary units. In association with chloritization and late-stage overprint of skarn assemblages, cassiterite is a common mineral and accounts for the majority of the tin mineralization within the Geyer skarns.

Stage I skarn

The skarnoid stage I skarns of the Geyer SW deposit occur as weakly delimited areas intercalated in the metasedimentary rocks and are composed predominantly of white to pale green, fine-crystalline clinopyroxene (Fig. 5d). Locally, euhedral brown to red garnet with sizes of up to several millimeters occurs as layers or aggregates that follow the metamorphic layering. This garnet is of the andradite-grossular series, shows only weak zonation and has abundant inclusions of pyroxene.

Pale red, lath-shaped vesuvianite accompanies pyroxene, garnet, and wollastonite. Commonly, vesuvianite and wollastonite replace garnet (Fig. 5d), which results in a very fine-grained texture. The skarn front (contact between skarn and marble) is marked by abundant wollastonite replacing calcite marble (Fig. 5e). Locally, euhedral, pale green epidote occurs at the contact between skarn and host rock. Titanite occurs regularly as euhedral minerals enclosed by garnet. Rutile and ilmenite of the metasedimentary rocks are replaced by titanite of the first skarn stage.

Fluorite is the most common non-silicate mineral in stage I skarn. It occurs throughout skarn I, comprising textures such as anhedral interstitial grains among clinopyroxene, infill between growth zones of garnet, and up to 0.6 mm large euhedral single grains coeval with vesuvianite.

Early skarn II stage

Stage II skarn contains significantly more garnet than stage I skarn, with clinopyroxene still being very abundant. This results in highly variable garnet/pyroxene ratios. In addition to the prominent vertical zoning within skarn layers (stage I at the margins and stage II in the center), skarn stage II also exhibits an internal mineralogical zoning. This zoning includes pyroxene- and vesuvianite-rich, fine-grained, massively textured rims almost without garnet. Toward the center of the skarn layers, the mineralogy becomes progressively coarser grained and enriched in garnet, with some garnet crystals reaching up to several centimeters size, whereas pyroxene crystals do not exceed a few millimeters in size (Fig. 4d). The metamorphic fabric of the host rocks is partly preserved in the pyroxene-vesuvianite rims of stage II skarn, whereas garnet-rich centers show an isometric texture without any remnant foliation. Almost monomineralic skarn layers consisting of vesuvianite or clinopyroxene and densely intergrown garnets are less affected by later replacement. Diopsidic to hedenbergitic clinopyroxene occurs as white to dark green acicular to columnar crystals (0.02 mm to 0.5 mm in length) that commonly form dense masses partly replacing stage I clinopyroxene (Fig. 5f). Stage II garnet belongs to the grossular-andradite solid solution series, which is highly variable with respect to size (µm- to cm-scale), color (red, beige, or green) and shape (euhedral and anhedral). This garnet generation truncates, cross-cuts, or overgrows previous garnet of skarn stage I (Fig. 5g).

Cores of garnet II form anhedral to euhedral crystals with more intense brown to reddish colors, weak growth zoning, and are optical anisotropic. The cores are commonly overgrown by rims of dark green to yellow garnet, exhibiting well defined growth zones and euhedral crystal shapes (Fig. 5h). Garnet II crystals may contain remnants of stage I garnet in their core.

Vesuvianite forms euhedral and lath-shaped crystals of reddish or greenish color, which are coeval to or postdate garnet II and which are commonly accompanied by fluorite. Vesuvianite of stage II fills fractures in and encloses vesuvianite I (Fig. 5i).

Malayaite, ($CaSnO[SiO_4]$), is the first tin-bearing mineral in the entire paragenetic sequence. It forms euhedral, lath-shaped crystals (<1 mm) that are intimately associated with

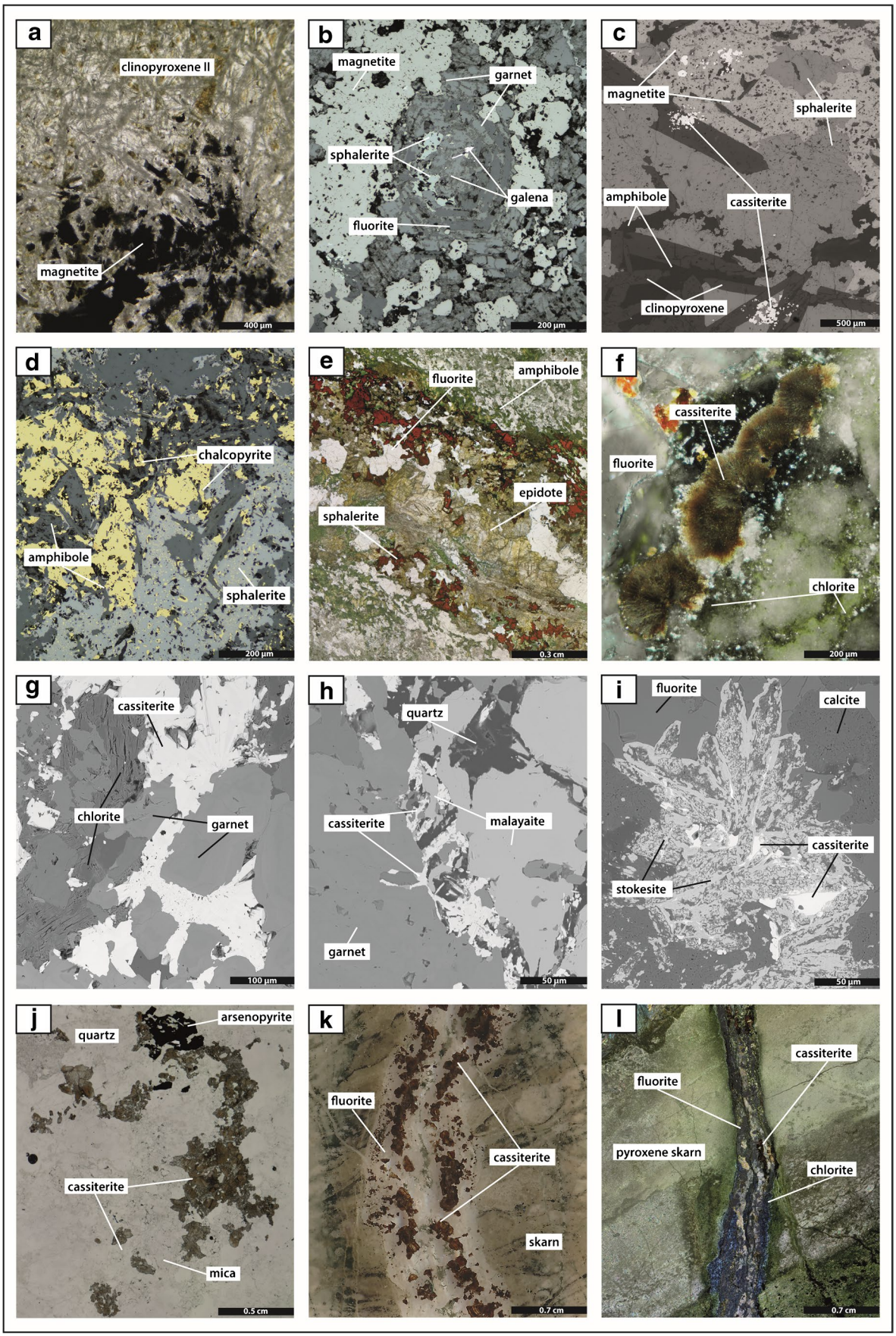
a
clinopyroxene II
magnetite
400 µm
b
magnetite
garnet
sphalerite
galena
fluorite
200 µm
c
magnetite
sphalerite
amphibole
cassiterite
clinopyroxene
500 µm
d
chalcopyrite
amphibole
sphalerite
200 µm
e
fluorite
amphibole
epidote
sphalerite
0.3 cm
f
cassiterite
fluorite
chlorite
200 µm
g
cassiterite
chlorite
garnet
100 µm
h
quartz
cassiterite
malayaite
garnet
50 µm
i
fluorite
calcite
cassiterite
stokesite
cassiterite
50 µm
j
quartz
arsenopyrite
cassiterite
mica
0.5 cm
k
fluorite
cassiterite
skarn
0.7 cm
l
cassiterite
fluorite
pyroxene skarn
chlorite
0.7 cm

◂**Fig. 6** Photomicrographs and backscattered electron microscopy images of common ore minerals and mineral textures. **a** Euhedral, diopside-rich clinopyroxene replaced by magnetite (GR-626-06c). **b** Magnetite, sphalerite, and minor galena replace garnet (GR-638-03a). **c** Euhedral clinopyroxene overgrown and partially replaced by magnetite, cassiterite, sphalerite, and amphibole (GR-626-06a). **d** Amphibole intergrown with chalcopyrite, sphalerite, and minor galena (GR-638-04a). **e** Epidote and amphibole accompanied by sphalerite and fluorite (GR-606-02a). **f** Anhedral to acicular wood-tin, fluorite, and chlorite in the late stage of skarn II alteration (GR-606-02a). **g** Cassiterite and chlorite fill fractures in garnet (GR-626-05a). **h** Malayaite enclosed by garnet is replaced by cassiterite and quartz (GM-1-08a). **i** Cassiterite replaced by stokesite and manganiferous calcite (GR-638-03c). **j** Greisenized granite with disseminated cassiterite (GR-R-148b). **k** Skarn cross-cut by a cassiterite fluorite and quartz vein (GR-657-02a). **l** Chlorite-fluorite-cassiterite vein cross-cuts pyroxene-skarn (GR-657-04a)

pyroxene, vesuvianite, and cores of grossular-rich garnet II (Fig. 5f, i, and j). Malayaite often replaces titanite (Fig. 5k) and occurs as lath-shaped, euhedral crystals enclosed by garnet and vesuvianite or occurs along growth zones of garnet. Early-stage skarn minerals are replaced by plagioclase and K-feldspar, at the end of the early skarn stage II. They are in turn overgrown by sericite, calcite, fluorite, and quartz (Fig. 5l).

Late-stage skarn II alteration

The transition to the late-stage phase of skarn II alteration (which affects both stage I and II skarns) is marked by the occurrence of magnetite, hydrous calc-silicates like epidote and amphibole as well as chlorite, minor base metal sulfides, and cassiterite. Magnetite occurs as coarse, crystalline, irregular pods, or interstitial grains enclosed by pyroxene (Fig. 6a). It is partially altered to hematite. It postdates clinopyroxene and garnet but predates amphibole and chlorite (Fig. 6b and c). Magnetite can be intergrown with spongy cassiterite, marking the first occurrence of this mineral in the mineral assemblage of the Geyer SW deposit and a variety of sulfide minerals like sphalerite, chalcopyrite, and galena. The latter, though, appear to be paragenetically younger than magnetite and associated cassiterite (Fig. 6d). Epidote forms dark green, prismatic crystals that exhibit distinct zoning. Epidote commonly occurs as lens-shaped to roundish aggregates together with fluorite and sometimes sphalerite (Fig. 6e). Modal abundances of epidote are highly variable, but it is usually present in both pyroxene-rich and garnet-rich skarn layers. Sphalerite, usually with chalcopyrite inclusions and coeval with independent chalcopyrite grains, is present as coarse-crystalline aggregates. Galena is almost invariably enclosed as anhedral inclusions in the other sulfides. Euhedral, greenish to black amphibole (<2 mm) is accompanied by fluorite, quartz, occasionally sulfide minerals, and acicular cassiterite (i.e., wood tin; Fig. 6f). Fine-grained green amphibole, however, occurs in pyroxene-dominated skarn and replaces clinopyroxene along veins and fractures. Euhedral cassiterite accompanied by chlorite and quartz fills fractures in garnet, vesuvianite, and clinopyroxene (Fig. 6g). There is evidence that cassiterite replaces malayaite (Fig. 6h). Minor amounts of fluorite and manganiferous hydrothermal calcite are the last minerals in the paragenetic sequence of skarn alteration. Calcite pseudomorphs after clinopyroxene are a characteristic feature of this stage, whereas garnets enclosing clinopyroxene remain unaffected by the replacement. In addition, Mn-calcite overgrows cassiterite; scarce stokesite (a rare Ca-Sn-hydrosilicate) is in close association with calcite (Fig. 6i).

Greisen alteration

Greisen alteration occurs mainly within the granitic intrusion at Geyer (endogreisen), but also extends into the metamorphic host rock (exogreisen). Greisen alteration at Geyer is mainly related to veins (<3 cm thickness) and dense stockwork zones (<6 m thickness) that result in extensive alteration zones. Greisen mineral association comprises mainly quartz, Li-mica, and topaz that replace igneous feldspar and mica, but also occur as vein infill. Cassiterite accompanies greisen minerals and occurs as disseminated grains in the alteration halos and in the veins (Fig. 6j). Sizes of cassiterite crystals are generally larger in veins than in pervasively altered areas. In addition, fluorite and apatite occur within veins. Minor wolframite, molybdenite, and loellingite intergrown with arsenopyrite were recognized.

Late-stage veins

Abundant veinlets, which range in thickness between 0.5 mm and 5 cm, cross-cut metasedimentary and skarn units (Fig. 4i). Veins of this type can be traced in drill cores over a length of up to 300 m. The mineralogy of the veins includes variable abundances of chlorite, quartz, fluorite, cassiterite, and arsenopyrite. Based on the predominant vein minerals, three different associations are observed: (a) chlorite-cassiterite, (b) fluorite-cassiterite, and (c) fluorite-quartz veins. Chlorite-cassiterite veins, which are typically accompanied by an alteration halo that reaches about five times the vein thickness, mainly occur within skarn units but may extend up to several centimeters into the metasedimentary units. They postdate skarn I and the early stage of skarn II and contain aggregates of euhedral chlorite (<200 µm), accompanied by subhedral fluorite crystals (<400 µm). Cassiterite occurs as euhedral zoned crystals with sizes <5 mm (Fig. 6k) and as massive dark brown aggregates interstitial between chlorite grains in the alteration halo (Fig. 6l). Locally, euhedral arsenopyrite is present together with anhedral quartz between fluorite and chlorite minerals. Fluorite-cassiterite

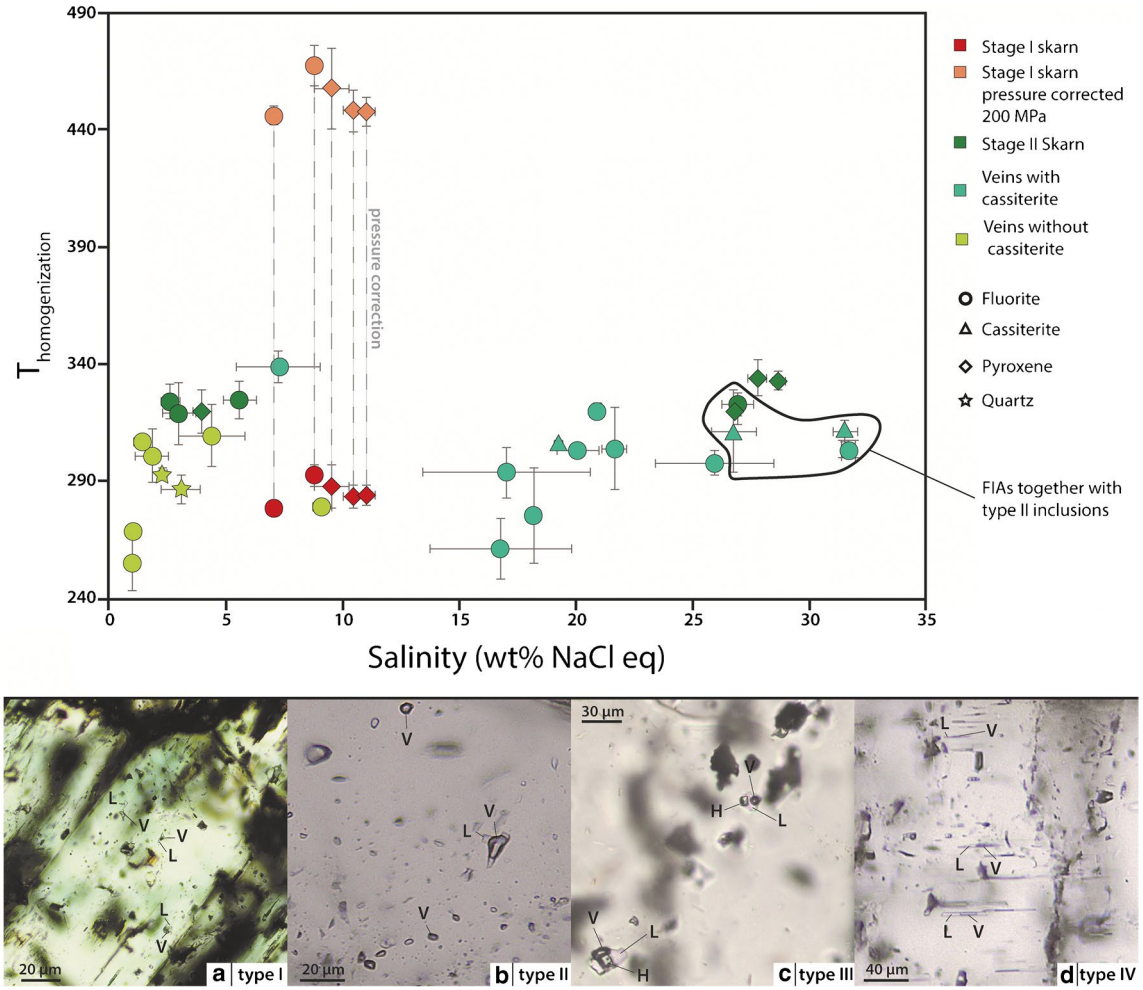

Fig. 7 Salinity (NaCl±$CaCl_2$) versus homogenization temperature in °C of analyzed fluid inclusion assemblages (FIAs). Data points show the average values of measured FIAs with corresponding error bars delineate the range of FIAs. FIAs are categorized according to the host mineral and the respective alteration stage. FIAs of stage I are pressure corrected assuming 200 MPa as formation pressure. **a** Type I liquid-rich two-phase primary fluid inclusions in green clinopyroxene. **b** Type II vapor-dominant fluid inclusions in fluorite. **c** Type III liquid-rich multiphase fluid inclusions in a pseudosecondary trail hosted by fluorite. **d** Type IV two-phase fluid inclusions in primary trails hosted by fluorite from a vein

Table 2 Summary of the microthermometric data of analyzed fluid inclusion assemblages from the Geyer system

Alteration stage	Host mineral	Fluid inclusion type	Petrography of fluid inclusion	# of FIAs	# fluid inclusions	Tm(ice) (°C) min/avg/max	Th (°C) uncorrected min/avg/max	Th (°C) P-corrected min/avg/max	Salinity in wt. % eq. (Nacl ± $CaCl_2$)
Stage I skarn[1]	cpx	Type I-L	ps	5	25	-7.4/-6.2/-4.4	279/285/293	447/ 454/468	7.06/9.37/11.00
Stage II skarn[2]	cpx, fl	Type I-L	p	4	23	-3.42/-2.27/-1.53	319/322/325	328/331/334	2.61/3.79/5.58
Stage II skarn[2]	cpx, fl	Type III-LVS	ps	4	19	-37.3/-32.8/-30.6	320/328/334	334/339/343	26.92/27.58/28.69
Veins with cst[2]	fl	Type I-L	p	1	9	- /-4.61/ -	- /339/ -	- /351/ -	- /7.27/ -
Veins with cst[2]	fl, cst	Type III-LVS	ps	11	67	-33.83/-21.87/-13.68	262/299/321	269/309/331	16.77/22.70/31.54
Veins without cst[2]	qz, fl	Type IV-LV	c, p	8	44	-5.93/-1.84/-0.55	255/288/310	272/300/318	0.96/3.02/9.12

Salinities were calculated according to Steele-MacInnis et al. (2012) for the H_2O-NaCl system and Steele-MacInnis et al. (2011) for the H_2O-NaCl-$CaCl_2$ system without taking potential CO_2 content into account. Min/avg/max values are given for fluid inclusion assemblages of one type in one alteration stage. Homogenization temperature was recalculated to a trapping pressure of [1]200 MPa and [2]15 MPa. *Cpx*, clinopyroxene; *fl*, fluorite; *cst*, cassiterite; *qz*, quartz; *p*, primary; *ps*, pseudosecondary; *c*, cluster

and fluorite-quartz veins do not show distinct alteration halos and share many similarities. The only obvious difference is that the former includes cassiterite, whereas the latter does not. The occurrence of these veins is not restricted to skarn horizons; they cross-cut skarn as well as metasedimentary units and granitic rocks. Minor mineral phases in these veins are scheelite and arsenopyrite. Due to their similar mineralogy, we assume that these two vein types are coeval and reflect local mineralogical varieties of the same stage. Fluorite±quartz±cassiterite veins postdate the main skarn stages (including chlorite-cassiterite veins), which indicates that they reflect the latest stage of tin mineralization.

Fluid inclusions

Fluid inclusion microthermometric results related to skarns, greisen, and veins are described within their petrographic context in the following section.

Petrography of fluid inclusions

Fluid inclusions (FI) suitable for microthermometry were detected in pyroxene, fluorite, quartz, and cassiterite of the various textural stages described above. In total, 187 fluid inclusions (excluding vapor-rich fluid inclusions) in 33 fluid inclusion assemblages (FIA) were analyzed. These included primary, pseudosecondary, and clustered inclusions (Goldstein and Reynolds 1994; Roedder 1984). Based on observations at room temperature (20 °C; and in cooling experiments in the case of hydrohalite), four types of fluid inclusions were distinguished (Fig. 7).

Type I-L FIs (fluid-rich two-phase FIs) contain a liquid (70–80 vol%) and a vapor phase (20–30 vol%). They are ellipsoid or irregular in shape and commonly occur in pseudosecondary trails. The diameter of the inclusions is highly variable, ranging from <10–55 µm.

Type II-V FIs (vapor-rich two-phase FIs) are characterized by a high proportion of vapor (>90 vol%). They are usually irregular or show the shape of a negative crystal, ranging between 10 and 25 µm in diameter, with a few exceptions of larger inclusions. This type is intimately associated with some FIAs of type III and occurs in the same primary or pseudosecondary trails.

Type III-LVS FIAs (liquid-rich multiphase FIs) contain an aqueous liquid phase (60–80 vol%), a vapor phase (20–40 vol%), and one or more daughter crystals. The diameter of the inclusions does not exceed 25 µm and the shape is ellipsoid, irregular, or angular. Solid phases in the FIs are halite or hydrohalite, and less commonly fluorite.

Type IV-LV FIAs (two-phase FIs) contain a liquid phase (40–60 vol%) and a vapor phase (40–60 vol.%). Primary inclusions appear as clusters in fluorite or in quartz. Also, pseudosecondary trails with roundish and elongated inclusions that cross-cut one or two growth zones in fluorite are present. The diameter of these inclusions varies from <5–45 µm.

Microthermometry of fluid inclusions

The microthermometric data of the different fluid inclusion types are summarized in Table 2. The data are presented and grouped according to the textural position of the host minerals within the different alteration assemblages. A detailed background data set including individual fluid inclusion analyses is provided in ESM Table 1.

Stage I skarn Fluid inclusion assemblages in cogenetic hedenbergite (Fig. 7a) and fluorite of stage I skarn show homogeneous entrapment and are invariably type I-L inclusions. The average eutectic temperature is 21 °C, so these fluid inclusions are best described in the NaCl-H_2O system. The homogenization temperature T_h (LV➔ L) ranges from 279–293 °C (uncorrected; 447 to 468 °C for estimated pressures, see discussion for more details). The melting temperature of ice $T_{m(ice)}$ is between −4.4 °C and −7.4 °C, corresponding to a salinity of 7.1–11.0 % eq. w(NaCl).

Skarn, greisen, and vein stage II In the stage II skarn, FIAs of type I-L, II-V, and III-LVS of the NaCl-H_2O system and of the NaCl-$CaCl_2$-H_2O system were identified in fluorite and clinopyroxene (Fig. 7). Type I-L FIAs show T_h (LV-L) of 320–325 °C, $T_{m(ice)}$ of −1.5 to −3.4 °C, which corresponds to a salinity range of 2.6 and 5.6% eq. w(NaCl). Fluid inclusions of type III-LVS in clinopyroxene and fluorite have T_h of 325 to 335 °C. $T_{m(ice)}$ ranges from −37.2 to −31.0 °C, and the melting temperature of hydrohalite ($T_{m(hh)}$) is between −32.0 and −16.5°C, which corresponds to a salinity of 26.9–28.7% eq. w(NaCl+$CaCl_2$). Type III-LVS can locally be found in the same trail as type II-V fluid inclusions.

In chlorite-cassiterite and fluorite-cassiterite veins, fluid inclusions of type I-L, II-V, and III-LVS of the NaCl-H_2O system and the NaCl-$CaCl_2$-H_2O system were observed in fluorite and cassiterite. In trails with type III-LVS inclusions, FIs of type II-V can occur, which indicates heterogeneous entrapment. Neither the T_h nor the Tm could be determined in these inclusions since the phase transitions were not visible due to the high content of the vapor phase (Fig. 7b). Halite-bearing type III-LVS inclusions (Fig. 7c) have T_h of 305–310 °C, melting temperatures of halite $T_{m(h)}$ between 120 and 140 °C, which results in an average salinity of 31.5% eq. w(NaCl+CaCl2). Halite-free type III-LVS inclusions have a T_h between 275 and 320 °C, a $T_{m(hh)}$ of −44.1 to −22.7 °C, and a corresponding salinity of 20.0–32.2% eq. w(NaCl+$CaCl_2$). Fluid inclusions of type III-LVS hosted by fluorite, which are best described in the H_2O-NaCl system, have an average T_h of 340 °C, $T_{m(ice)}$ of −4.6°C, and a

salinity of 7.3% eq. w(NaCl). In veins without cassiterite, fluid inclusions of type IV-LV, also best described in the H_2O-NaCl-system, were analyzed in fluorite (Fig. 7d) and quartz. The latter contains inclusions with a T_h of 285–295 °C, $T_{m(ice)}$ between −1.8 and 1.3 °C, corresponding to a salinity of 2.3–3.1% eq. w(NaCl). Fluorite contains fluid inclusions with T_h of 255 to 310 °C, $T_{m(ice)}$ between 0.6 and 5.9°C, and a resulting salinity of 1.0–5.9% eq. w(NaCl).

Geochronology

Five garnet samples with 144 and three cassiterite samples with 95 individual spot analyses were successfully dated by U-Pb LA-ICP-MS. The concentration of U and Pb and the calculated ages, sample location, and number of spot analyses are compiled in Table 1.

Samples GR4 (drill core Z626, 85 m) and GR5 (drill core Z606A, 79.5 m) are related to stage I skarn. The analyzed reddish to brown garnet is of grossular-rich grandite composition, accompanied by green to white, diopsidic clinopyroxene (Fig. 2a). Samples GR4 and GR5 contain only prograde calc-silicate minerals and there is no evidence of chloritization. The U content of garnet in sample GR4 ranges from 0.04–0.65 µg/g and in GR5 from 0.01–1.75 µg/g, and Pb concentrations in garnets range from 0.01–0.14 µg/g in GR4 and 0.06–0.39 µg/g in GR5. Results from these two samples yield overlapping lower intercept ages of 322.4 ± 5.1 Ma and 322.1 ± 11.8 Ma, respectively (Fig. 2a).

The garnet samples GR1 (96.5 m), GR2 (59 m), and GR6 (45.6 m) from drill core Z626 (Fig. 2b) are related to stage II skarn. Garnets in these samples are pale to dark green, andradite-rich and are intergrown with clinopyroxene. Samples GR2 and GR6 contain prograde minerals only, whereas GR1 is cross-cut by some thin chlorite veins (<1 mm). The U contents of the garnets in these samples vary between 0.01 µg/g and 1.4 µg/g, and Pb concentrations vary between 0.01 µg/g and 0.9 µg/g. The U-Pb data yield lower intercept ages of 307.3 ± 4.8, 305.1 ± 3.9, and 301.6 ± 5.0 Ma for samples GR6, GR2, and GR1, respectively. Cassiterite from sample GR657-02a (core Z657, 83.8 m) occurs in a vein accompanied by fluorite and quartz cross-cutting a skarn (Fig. 2c). The cassiterite is euhedral and exhibits distinct growth zones with dark brown to translucent domains. The U and Pb content of the cassiterite ranges between 1.4–16.5 µg/g and 0.08–1.2 µg/g, respectively. The U-Pb data result in a lower intercept age of 308.2 ± 3.7 Ma. Samples 60973 and 60974 ("Binge," Geyer) contain granite-hosted greisen with cassiterite closely associated with quartz, mica, and topaz (Fig. 2d). The U content of these cassiterite crystals ranges from 0.09–33.1 µg/g, with a Pb content between 0.06 and 14.1 µg/g, yielding a lower intercept age of 305.7 ± 3.7 and 306.6 ± 3.5 Ma, i.e., within the error of the ages obtained for cassiterite from veins and from garnets of skarn II assemblages.

Discussion

In the following, the geochronological data of garnet and cassiterite as well as cross-cutting relationships are discussed to constrain the temporal evolution of the Geyer magmatic-hydrothermal system. Furthermore, the geochronological data is used to evaluate potential causative intrusions in the area and to integrate the timing of hydrothermal activity at Geyer into the existing geochronological framework of the Erzgebirge region. Fluid inclusion data is used to constrain the fluid evolution of the magmatic-hydrothermal system, providing important clues to better understand hydrothermal tin enrichment in Variscan skarn systems.

Temporal evolution of the Geyer magmatic-hydrothermal system

In situ U-Pb geochronology on garnet yields an age of 322.4 ± 5.5 (GR4) and of 322.5 ± 11.4 Ma (GR5) for the stage I skarns, coinciding with the emplacement of the nearby Greifenstein intrusion, which was dated to 324 ± 4 to 320 ± 3 (Romer et al. 2007) and the early stage of emplacement of the large-volume Eibenstock granite intrusion, with an age range between 323 and 314 Ma (Förster et al. 2009; Kempe et al. 2004; Tichomirowa et al. 2019; Warkus 1997). This relates the formation of stage I skarns to the emplacement of the major batholiths in the area.

Stage II skarn garnet ages of 307 ± 5, 305 ± 4, and 301.6 ± 6 Ma are invariably younger than skarnoid garnet of stage I skarn, consistent with textural observations. Cassiterite ages of 305.7 ± 2.8, 306.6 ± 2.5 Ma (both greisen), and 308.2 ± 2.9 Ma (late-stage vein) relate stage II skarn, greisen alteration, and late-stage veins to the same magmatic-hydrothermal event which clearly postdates the emplacement of the known granitic intrusions in the area (Romer et al. 2007). This suggests that tin mineralization is related to a younger, yet previously unrecognized magmatic event (Fig. 8). The fine-grained quartz-topaz-rich intrusion and the rhyolitic dykes (Bolduan 1963a) that postdate the main intrusive stage at Geyer support this assumption, as these rocks are most likely related to the causative intrusions for tin mineralization. However, direct geochronological data that constrain the timing of these younger intrusions are unfortunately not available at Geyer.

The observation that hydrothermal mineralization postdates the emplacement of the large-volume intrusions (e.g., Eibenstock) in the Geyer district is consistent with the timing of skarn formation and magmatic-hydrothermal activity recently constrained in a regional reconnaissance study

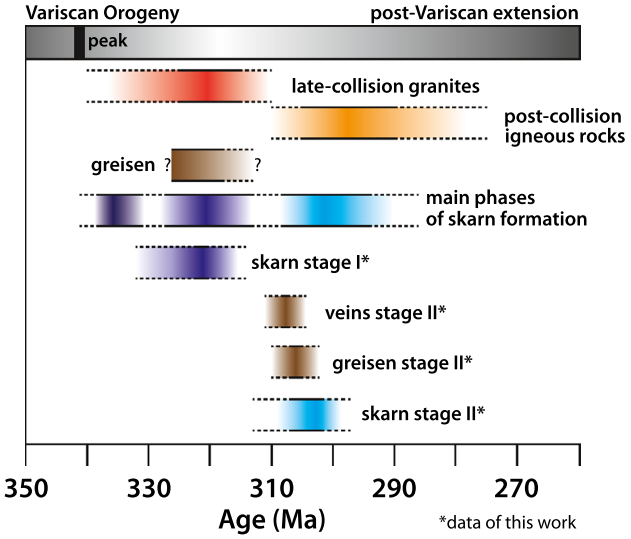

Fig. 8 Geodynamic overview and compilation of geochronological data of igneous rocks of the Erzgebirge and hydrothermal mineralization (after Reinhardt et al. 2022 and references therein). Data of this study is shown separately and marked with an asterisk

of skarns in the Erzgebirge metallogenic province (Burisch et al. 2019) as well as a geochronological study of skarns in the Schwarzenberg district further to the west (Reinhardt et al. 2022). Both studies recognized three distinct episodes: (A) 338–331 Ma, (B) 327–310 Ma, and (C) ~310–295 Ma.

Whereas stages A and B may be related to the emplacement of late-collisional granites, stage C coincides with post-collisional magmatic activity in the region (Förster et al. 1999; Hoffmann et al. 2013; Kröner and Willner 1998; Löcse et al. 2023; Luthardt et al. 2018).

The statistically robust age difference between stage I and stage II skarn, greisen, and veins suggests a distinct hiatus in the magmatic and magmatic-hydrothermal activity in the Geyer district of at least 12 Ma. Skarn deposits of the Schwarzenberg district show similar characteristics with an early-stage coinciding with the emplacement of large granitic batholiths in the area — and a distinctively younger skarn stage that is associated with extensive retrograde alteration and magmatic-hydrothermal mineralization. This bimodal age distribution seems thus to be a common feature in Erzgebirge skarn deposits (Burisch et al. 2019; Reinhardt et al. 2022), but rather atypical for skarn deposits in general (e.g., Burisch et al. 2023; Meinert et al. 2005).

Finally, it is important to point out that ages obtained for greisen- and skarn-hosted cassiterite in this study provide the first direct evidence that greisen- and skarn-type mineralization in the Erzgebirge are of similar age — and, hence, most likely related to the same magmatic-hydrothermal event (Figs. 8 and 9). Furthermore, the new ages document that formation of greisen-hosted tin mineralization in the Erzgebirge does not (only) coincide with late-collisional (Zhang et al. 2017) but (also) with post-collisional magmatic activity.

Genesis of the Geyer magmatic-hydrothermal system

Stage I

Geochronological data relate stage I skarn to the emplacement of the large late-collisional granitic batholith at ~324–315 Ma. Characteristically red garnet and pale green pyroxene of skarn I are typical of skarns that form relatively proximal to their causative intrusion (Fig. 9). The fine-crystalline nature and skarnoid texture indicate formation under almost contact-metamorphic conditions, with only limited hydrothermal fluid involved, related to the thermal anomaly associated with the emplacement of the batholith (Meinert et al. 2005; Papeschi et al. 2017). The low amount of fluid involved in stage I skarn formation is furthermore supported by the distinct absence of a stage associated with hydrous skarn minerals. Based on these considerations, the emplacement depth of the genetically associated intrusion should provide a good estimate for the depth of formation of stage I skarn. The nearby Greifensteine intrusion was emplaced at a depth between 2.5 and 4.0 km at a minimum pressure of 200 MPa (Breiter et al. 1999; Romer et al. 2007), which is assumed to also correspond to the Geyer intrusion. Since contact metamorphic and ductile conditions probably prevailed during this stage, we assume lithostatic conditions during the formation of stage I skarn. Consequently, fluid inclusion homogenization temperatures were corrected for pressures of 200 MPa (Fig. 7). This results in a formation temperature for stage I skarn of 450–470 °C, involving fluids with intermediate salinities, which is consistent with early-stage magmatic fluids that exsolve from granitic magmas (Driesner and Heinrich 2007; Korges et al. 2020). The absence of cassiterite and tin silicates associated with stage I skarn is likely related to one or more of the following factors: (a) formation of skarn stage I predates the main fluid exsolution event and (b) magmatic fractionation during the formation of skarn I stage was not sufficient to efficiently enrich tin in the associated fluids, which has been proposed to be a key factor for the formation of tin deposits (Simons et al. 2017; Taylor 1979).

Stage II skarn, greisen, and late-stage vein formation

In contrast to skarn I, skarn II shows distinct features that imply relatively distal and shallow formation conditions (Fig. 9) under hydrostatic pressure (mainly following the arguments of Meinert et al. 2005). These features include the abundance of green garnet as well as vein and cavity textures of skarn II. Using boiling assemblages, minimum

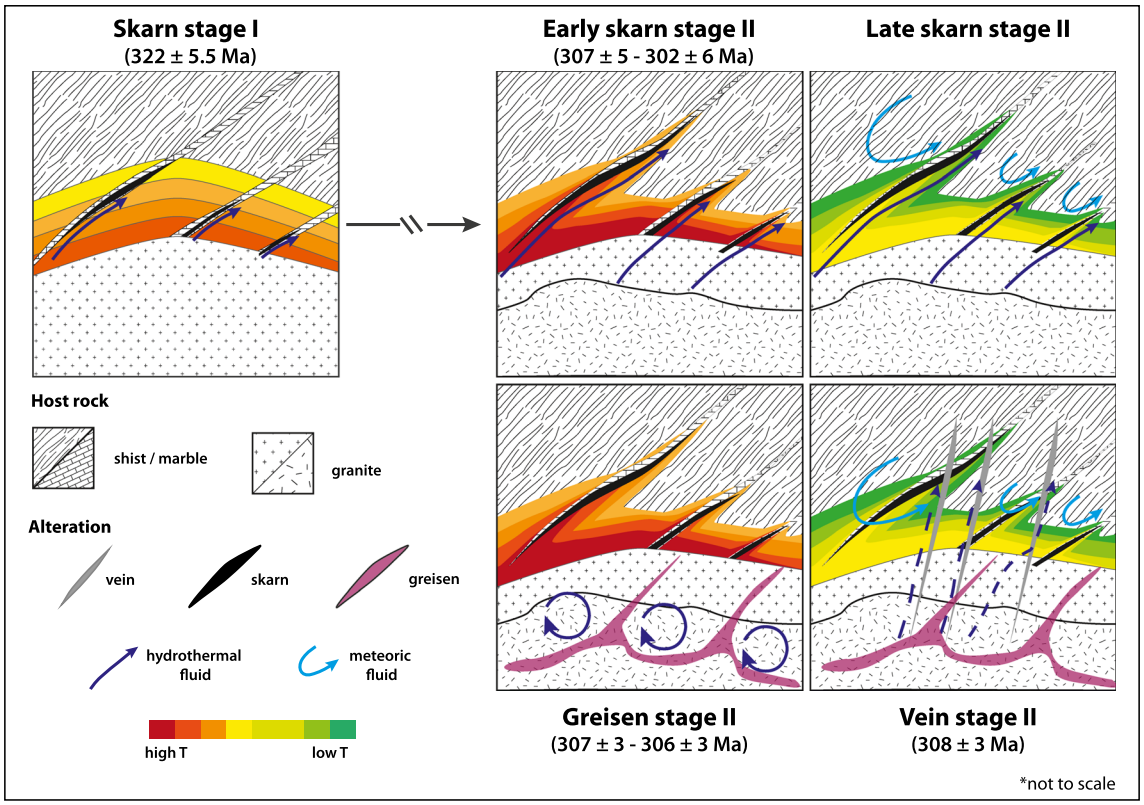

Fig. 9 Schematic genetic model illustrating the spatial and temporal evolution of the Geyer magmatic-hydrothermal system (not to scale)

pressures for the entrapment of fluid inclusions related to skarn stage II yield 10–15 MPa. Assuming hydrostatic conditions, these pressures correspond to formation depths of 1.5–2 km below the paleo water table (Driesner and Heinrich 2007). The differences between the depth of formation between stage I skarn (4.0–2.5 km) and stage II skarn are consistent with the fast tectonic uplift of the Erzgebirge that followed the collisional stage of the Variscides (Burisch et al. 2019; Schmädicke et al. 1995). A similar present-day position, but different formation conditions of skarn stage II and I suggest that the unknown causative granitic intrusion (fluid source) of skarn II can be expected to be a small (?), subvolcanic granite stock, similar to those exposed in the Eastern Erzgebirge (e. g. Zinnwald-Cinovec, Altenberg).

Fluid inclusion data suggest that the onset of skarn II formation occurred at >330 °C. Fluid inclusions related to the early stage of skarn II show a bimodal salinity distribution (Fig. 7). FIAs with low salinity do not show any indication for heterogeneous entrapment or phase separation. Therefore, these inclusions are interpreted to display the unmodified skarn-forming fluid. The occurrence of high-salinity fluid inclusion assemblages with indications of heterogeneous entrapment indicates that boiling occurred, whereas ingress of larger amounts of meteoric fluids during the early stage is unlikely (Fekete et al. 2016). Fluid salinities above ~20 wt% seem to be characteristic of the early stages of greisen- and skarn-hosted tin deposits in general (Korges et al. 2018, 2020; Peng and Bromley 1992). This is consistent with numerical hydraulic models (Fekete et al. 2016) that suggest that overpressure during the early stage inhibits entrainment of significant amounts of meteoric fluids into the magmatic-hydrothermal system.

Fluid inclusion homogenization temperatures could not be measured in minerals related to late-stage skarn II alteration, but a continuous cooling trend (340 to 240 °C) is recognized between skarn stage II and late-stage veins (Fig. 7). This cooling trend coincides with the transition from early- to late-phase skarn II formation and late-stage veining. Cooling has to be considered as a main controlling factor for base metal sulfide and cassiterite precipitation according to thermodynamic modeling and the relationship between ore and gangue minerals, as described in other skarn systems (Bertelli et al. 2009; Einaudi et al. 1981; Reed 2006). External input of sulfide from the metasedimentary host rock cannot be excluded.

The large range in salinities in fluid inclusions related to late veins suggests a continuous mixing trend of the highly saline magmatic-hydrothermal fluid with a diluted (probably meteoric) fluid during this late-stage evolution of the Geyer system. Since a clear correlation between

salinity and temperature is lacking, it is likely that the meteoric fluids were heated up in the magmatic-hydrothermal system prior to entrainment (Audétat et al. 2000). The salinity and homogenization temperature of fluid inclusions from veins are consistent with fluid inclusions analyzed in greisen-hosted fluorite, which furthermore supports that greisen, skarn, and vein mineralization at Geyer are all different expressions of the same magmatic-hydrothermal event. Hence, the host rocks (igneous, marble, or mica schist) and cooling related to the temporal evolution of magmatic-hydrothermal tin systems are key factors that control the style of alteration and mineralization. At Geyer, younger hydrothermal fluorite quartz veins occur. The lack of cassiterite, epidote, and chlorite and significantly lower fluid inclusion homogenization temperatures (~110–170 °C) indicates that those veins are unrelated to tin mineralization.

Tin mineralization

The presence of malayaite in early skarn stage II marks the first enrichment of tin in the Geyer SW deposit. Backed by the cassiterite and garnet ages (308–302 Ma), this clearly indicates that tin mineralization is not associated with the emplacement of the large-volume batholith of the area, but is instead related to a probably more fractionated, smaller intrusion emplaced relatively more distal/deeper below the Geyer skarn system. The lack of tin silicates and the scarcity of distinct tin-bearing minerals in stage I skarn support a magmatic-hydrothermal source of tin and argue against local remobilization of tin from adjacent meta-sedimentary host rock units, as was recently proposed by (Lefebvre et al. 2019). The appearance of tin-rich silicates in early-stage skarn II assemblages rather indicates that tin was scavenged from an early-stage magmatic-hydrothermal fluid. This early-stage fixation in stage II skarn inhibited dispersion and promoted local concentration of tin in skarn layers.

A distinctly higher salinity of fluids related to cassiterite-bearing veins and greisen-altered domains compared to veins and greisen that are cassiterite-free indicates that chlorinity may have played a key role for cassiterite precipitation (Heinrich 1990) as tin is effectively transported as Sn-chloro-complexes (Schmidt 2018). The significant increase in salinity from about 4 to about 27 % eq. w($NaCl+CaCl_2$) appears to have been related to boiling of the early magmatic-hydrothermal fluid. Subsequent dilution and potentially concomitant cooling of chlorine-rich ore fluids are proposed as the controlling factor for cassiterite precipitation, which has been previously proposed as an efficient mechanism for tin enrichment in magmatic-hydrothermal systems (Audétat et al. 2000). The mineralogy and microthermometric data of cassiterite-free fluorite-quartz veins provide robust evidence that these veins do not belong to later Mesozoic mineralization styles, but instead imply that they are genetically related to the magmatic-hydrothermal stage. Therefore, we propose that such cassiterite-free fluorite-quartz veins likely formed from fluids which were along the fluid flow path already depleted in tin. Replacement of tin-bearing silicates by late-stage chlorite, actinolite, and calcite provided an additional source of tin, which promoted local enrichment of cassiterite and/or wood tin during the latest stages of the system.

Conclusions

The magmatic-hydrothermal tin deposit of Geyer, Erzgebirge, eastern Germany, shows various mineralization styles hosting tin ore minerals: greisen alteration restricted to the magmatic host rocks and skarns formed from former marbles and late-stage veins. The skarns occur as laterally extensive units comprised of several individual discontinuous skarn lenses replacing the marble of the metamorphic successions of the district. Mineral textures and cross-cutting relationships indicate two separate skarn-forming events — very similar to the observations made recently for skarn deposits of the Schwarzenberg district in the Erzgebirge (Reinhardt et al. 2021).

LA-ICP-MS U-Pb age dating of cassiterite and garnet was employed to constrain the temporal evolution of the magmatic-hydrothermal system at Geyer. The data provide the first direct evidence that greisen, skarn, and vein-type tin mineralization within one district/deposit in the Erzgebirge are different mineralogical expressions of the same magmatic-hydrothermal system.

The first skarn stage is not associated with any tin mineralization, shows characteristics of a proximal contact metamorphic skarn that formed under lithostatic conditions at probably 4 to 2.5 km depth, and coincides with the emplacement of large-volume batholiths in the area at around 320 Ma. Tin mineralization (malayaite and cassiterite) is, however, associated with the second, distinctly younger skarn-forming event at around 305 Ma. The formation depth of this skarn stage II is estimated to 2 to 1.5 km This shallower depth compared to skarn stage I is consistent with extensive uplift that occurred in the Erzgebirge between 320 and 305 Ma (Schmädicke et al. 1995). Although granitic intrusions coeval to skarn stage II are not documented in the area, there are abundant volcanic rocks of that age documented across the Erzgebirge. Hence, formation of skarn stage II is tentatively related to a younger and deeper intrusion. Based on fluid inclusion and petrographic observations, cooling and dilution of late-stage fluids by meteoric water is proposed as the key mechanism for cassiterite precipitation, that is mainly associated with late-stage chlorite-actinolite alteration and veining. The garnet/clinopyroxene ratio and colors of calc-silicates, the late occurrence of cassiterite in the paragenetic sequence, and the geometry of the skarn stage II at Geyer (and other

skarns in the Erzgebirge) are different from classic, very proximal tin skarns (Kwak 1987). Instead, their mineralogy and fluid inclusion systematics suggest a more distal environment relative to the causative source intrusion. In contrast to classical skarn occurrences worldwide (Meinert et al. 2005), a systematic zoning of garnet/clinopyroxene ratios or a color change in the calc-silicates cannot be observed within the Geyer skarns. The lack of zoning is likely related to the large size of the system, and therefore, the recognition of zoning on a larger scale would require an even more extensive lateral grid of sampling (cf. Reinhardt et al. 2021).

Supplementary Information The online version contains supplementary material available at https://doi.org/10.1007/s00126-023-01194-8.

Acknowledgements We would like to thank Rongqing Zhang and two anonymous reviewers for their constructive comments that improved an earlier version of this manuscript. Manuel Lapp (LfULG Sachsen) is thanked for providing access to drill cores, thin sections, and exploration reports. We are grateful to Roland Würkert (Helmholtz Institute for Resource Technology) for sample preparation. Richard Albert is thanked for scans and support with geochronological measurements. This is FIERCE contribution No. 137.

Funding Open Access funding enabled and organized by Projekt DEAL. This project is financially supported by the German Science Foundation DFG via grant 3134023001 and 441189074 in the framework of the SPP 2238 DOME.

Declarations

Competing interests The authors declare no competing interests.

References

Audétat A, Günther D, Heinrich CA (2000) Causes for large-scale metal zonation around mineralized plutons: fluid inclusion LA-ICP-MS evidence from the Mole Granite, Australia. Econ Geol 95:1563–1581. https://doi.org/10.2113/gsecongeo.95.8.1563

Bauer ME, Seifert T, Burisch M, Krause J, Richter N, Gutzmer J (2019) Indium-bearing sulfides from the Hämmerlein skarn deposit, Erzgebirge, Germany: evidence for late-stage diffusion of indium into sphalerite. Miner Deposita 54:175–192

Bertelli M, Baker T, Cleverley JS, Ulrich T (2009) Geochemical modelling of a Zn–Pb skarn: constraints from LA–ICP–MS analysis of fluid inclusions. J Geochem Expl 102:13–26. https://doi.org/10.1016/j.gexplo.2008.11.015

Bolduan H (1963a) Geologie und Genese der Zinn-Wolframlagerstätte Geyer (Erzgeb.). Freiberger Forsch-Hefte C 167:7–34

Bolduan H (1963b) Geologische Ergebnisse von Bohrungen auf verdeckte Granitaufwölbungen im Raum Geyer-Ehrenfriedersdorf. Freiberger Forsch-Hefte C 167:95–105

Breiter K, Förster H-J, Seltmann R (1999) Variscan silicic magmatism and related tin-tungsten mineralization in the Erzgebirge-Slavkovský les metallogenic province. Miner Deposita 34:505–521. https://doi.org/10.1007/s001260050217

Breiter K, Ďurišová J, Hrstka T, Korbelová Z, Hložková Vaňková M, Vašinová Galiová M, Kanický V, Rambousek P, Knésl I, Dobeš P, Dosbaba M (2017) Assessment of magmatic vs. metasomatic processes in rare-metal granites: a case study of the Cínovec/Zinnwald Sn–W–Li deposit. Central Europe Lithos 292-293:198–217. https://doi.org/10.1016/j.lithos.2017.08.015

Burisch M, Gerdes A, Meinert LD, Albert R, Seifert T, Gutzmer J (2019) The essence of time – fertile skarn formation in the Variscan orogenic belt. Earth Planet Sci Lett 519:165–170. https://doi.org/10.1016/j.epsl.2019.05.015

Burisch M, Frenzel M, Seibel H, Gruber A, Oelze M, Pfänder JA, Sanchez-Garrido C, Gutzmer J (2021) Li-Co–Ni-Mn-(REE) veins of the Western Erzgebirge, Germany—a potential source of battery raw materials. Miner Deposita 56:1223–1238. https://doi.org/10.1007/s00126-021-01061-4

Burisch M, Markl G, Gutzmer J (2022) Breakup with benefits - hydrothermal mineral systems related to the disintegration of a supercontinent. Earth Planet Sci Lett 580:117373. https://doi.org/10.1016/j.epsl.2022.117373

Burisch M, Bussey SD, Landon N, Nasi C, Kakarieka A, Gerdes A, Albert R, Stein HJ, Gabites JA, Friedman RM, Meinert LD (2023) Timing of magmatism and skarn formation at the Limon, Guajes, and Media Luna gold ± copper skarn deposits at Morelos, Guerrero State, Mexico. Econ Geol 118:695–718. https://doi.org/10.5382/econgeo.4985

Černý P (1991) Fertile granites of Precambrian rare-element pegmatite fields: is geochemistry controlled by tectonic setting or source lithologies? Precamb Res 51:429–468. https://doi.org/10.1016/0301-9268(91)90111-M

Chen J, Halls C, Stanley CJ (1992) Tin-bearing skarns of South China: geological setting and mineralogy. Ore Geol Rev 7:225–248. https://doi.org/10.1016/0169-1368(92)90006-7

Driesner T, Heinrich CA (2007) The system H_2O–NaCl. Part I: correlation formulae for phase relations in temperature–pressure–composition space from 0 to 1000°C, 0 to 5000 bar, and 0 to 1 XNaCl. Geochim Cosmochim Acta 71:4880–4901. https://doi.org/10.1016/j.gca.2006.01.033

Einaudi MT, Meinert LD, Newberry RJ (1981) Skarn deposits. Econ Geol. https://doi.org/10.5382/AV75.11

Elsner H (2014) Zinn - Angebot und Nachfrage bis 2020, 2014th edn. DERA Rohstoffinformationen, 20. DERA, Berlin

Fekete S, Weis P, Driesner T, Bouvier A-S, Baumgartner L, Heinrich CA (2016) Contrasting hydrological processes of meteoric water incursion during magmatic–hydrothermal ore deposition: an oxygen isotope study by ion microprobe. Earth Planet Sci Lett 451:263–271. https://doi.org/10.1016/j.epsl.2016.07.009

Förster H-J, Tischendorf G, Trumbull RB, Gottesmann B (1999) Late-collisional granites in the Variscan Erzgebirge, Germany. J Petrol 40:1613–1645. https://doi.org/10.1093/petroj/40.11.1613

Förster HJ, Romer RL, Gottesmann B, Tischendorf G, Rhede D (2009) Are the granites of the Aue-Schwarzenberg Zone (Erzgebirge, Germany) a major source for metalliferous ore deposits? A geochemical, Sr-Nd-Pb isotopic, and geochronological study. N Jb Mineral Abh 186:163–184

Gerdes A, Zeh A (2006) Combined U–Pb and Hf isotope LA-(MC-) ICP-MS analyses of detrital zircons: comparison with SHRIMP and new constraints for the provenance and age of an Armorican metasediment in Central Germany. Earth Planet Sci Lett 249:47–61. https://doi.org/10.1016/j.epsl.2006.06.039

Gerdes A, Zeh A (2009) Zircon formation versus zircon alteration — new insights from combined U–Pb and Lu–Hf in-situ LA-ICP-MS analyses, and consequences for the interpretation of Archean zircon from the Central Zone of the Limpopo Belt. Chem Geol 261:230–243. https://doi.org/10.1016/j.chemgeo.2008.03.005

Goldstein RH, Reynolds TJ (1994) Systematics of fluid inclusions in diagenetic materials. SEPM Society for Sedimentary Geology, Tulsa, Okla

Guilcher M, Albert R, Gerdes A, Gutzmer J, Burisch M (2021) Timing of native metal-arsenide (Ag-Bi-Co-Ni-As±U) veins in continental rift zones – in situ U-Pb geochronology of carbonates from the Erzgebirge/Krušné Hory province. Chem Geol 584:120476. https://doi.org/10.1016/j.chemgeo.2021.120476

Haschke S, Gutzmer J, Wohlgemuth-Ueberwasser CC, Kraemer D, Burisch M (2021) The Niederschlag fluorite-(barite) deposit, Erzgebirge/Germany—a fluid inclusion and trace element study. Miner Deposita 56:1071–1086. https://doi.org/10.1007/s00126-020-01035-y

Heinrich CA (1990) The chemistry of hydrothermal tin(-tungsten) ore deposition. Econ Geol 85:457–481. https://doi.org/10.2113/gsecongeo.85.3.457

Hermann G (1967) Die Granite des Westerzgebirges und des Vogtlandes und ihre Beziehungen zu granitischen Gesteinen benachbarter Räume (Unpubl PhD thesis). Bergakademie Freiberg, Freiberg, p 205p

Hoffmann U, Breitkreuz C, Breiter K, Sergeev S, Stanek K, Tichomirowa M (2013) Carboniferous–Permian volcanic evolution in Central Europe—U/Pb ages of volcanic rocks in Saxony (Germany) and northern Bohemia (Czech Republic). Int J Earth Sci (Geol Rundsch) 102:73–99. https://doi.org/10.1007/s00531-012-0791-2

Hösel G, Fritsch E, Josiger U, Wolf P (1996) Das Lagerstättengebiet Geyer. Bergbau in Sachsen, 4. Sächsisches Druck- und Verlagshaus GmbH, Dresden

Hösel G (1994) Das Zinnerz-Lagerstättengebiet Ehrenfriedersdorf/Erzgebirge. Bergbau in Sachsen, 1. Sächsisches Druck- und Verlagshaus GmbH, Dresden

Hösel G (2002) Die polymetallische Skarnlagerstätte Pöhla-Globenstein. Bergbau in Sachsen, 8. Sächsisches Druck- und Verlagshaus GmbH, Dresden

Hoth K, Wolf P (1986) Pinge Geyer, Geologische Situation übertage, M 1 : 1000. Internal report, VEB GFE Freiberg,

Jackson NJ (1979) Geology of the Cornubian tin field 'a review'. Bull Geol Surv Malaysia 11:209–237. https://doi.org/10.7186/bgsm11197909

Kempe U, Bombach K, Matukov D, Schlothauer T, Hutschenreuter J, Wolf D, Sergeev S (2004) Pb/Pb and U/Pb zircon dating of subvolcanic rhyolite as a time marker for Hercynian granite magmatism and Sn mineralisation in the Eibenstock granite, Erzgebirge, Germany: considering effects of zircon alteration. Miner Deposita 39:646–669

Kern M, Kästner J, Tolosana-Delgado R, Jeske T, Gutzmer J (2019) The inherent link between ore formation and geometallurgy as documented by complex tin mineralization at the Hämmerlein deposit (Erzgebirge, Germany). Miner Deposita 54:683–698. https://doi.org/10.1007/s00126-018-0832-2

Korges M, Weis P, Lüders V, Laurent O (2018) Depressurization and boiling of a single magmatic fluid as a mechanism for tin-tungsten deposit formation. Geology 46:75–78. https://doi.org/10.1130/G39601.1

Korges M, Weis P, Lüders V, Laurent O (2020) Sequential evolution of Sn–Zn–In mineralization at the skarn-hosted Hämmerlein deposit, Erzgebirge, Germany, from fluid inclusions in ore and gangue minerals. Miner Deposita 55:937–952. https://doi.org/10.1007/s00126-019-00905-4

Kröner A, Willner AP (1998) Time of formation and peak of Variscan HP-HT metamorphism of quartz-feldspar rocks in the central Erzgebirge, Saxony, Germany. Contrib Mineral Petrol 132:1–20. https://doi.org/10.1007/s004100050401

Kuschka E (1994) Zur Mineralisation und Minerogenie der hydrothermalen Mineralgänge des Vogtlandes, Erzgebirges und Granulitgebirges. PhD thesis. TU Bergakademie Freiberg

Kwak TAP (1987) W-Sn skarn deposits, and related metamorphic skarns and granitoids. Elsevier, p 451

Lefebvre MG, Romer RL, Glodny J, Kroner U, Roscher M (2019) The Hämmerlein skarn-hosted polymetallic deposit and the Eibenstock granite associated greisen, western Erzgebirge, Germany: two phases of mineralization—two Sn sources. Miner Deposita 54:193–216. https://doi.org/10.1007/s00126-018-0830-4

Legler C (1985) Die schichtgebundenen Mineralisationen des Erzgebirges. Freib Forsch-Hefte C401 (Top. Report of IAGOD). Vol. XIV:93

Lehmann B (1990) Metallogeny of tin. Springer, p 211

Lehmann B (2021) Formation of tin ore deposits: a reassessment. Lithos 402-403:105756. https://doi.org/10.1016/j.lithos.2020.105756

Löcse F, Schneider G, Linnemann U, Rößler R (2023) Carboniferous–Permian volcanic evolution in the mid-European Variscides: U-Pb LA-ICP-MS zircon ages, geochemical and petrographical constraints from the NW Saxonian Volcanic Basin (Germany). Z Dt Ges Geowiss 174:7–30. https://doi.org/10.1127/zdgg/2023/0359

Lorenz W, Hoth K (1967) Räumliche Gesetzmäßigkeiten der Skarnverbreitung im Erzgebirge (Geologische Fragen der Skarnprognose im Erzgebirge - Teil 2). Geologie 16:1007–1030

Luthardt L, Hofmann M, Linnemann U, Gerdes A, Marko L, Rößler R (2018) A new U–Pb zircon age and a volcanogenic model for the early Permian Chemnitz Fossil Forest. Int J Earth Sci (Geol Rundsch) 107:2465–2489. https://doi.org/10.1007/s00531-018-1608-8

Makarevič W, Fritsch E, Velickin W, Kargatev W, Ivanov I, Serov B, Nasarov WG, Lohrmann H (1976) Über die Ergebnisse der geologischen Erkundungsarbeiten im Bereich der Lagerstätte Geyer einschließlich der Vorratsberechnung auf Zinn mit Stand vom 1. Juli 1976. Internal report, SDAG Wismut Chemnitz

Meinert LD, Dipple GM, Nicolescu S (2005) World skarn deposits. In: Hedenquist JW, Thompson JFH, Goldfarb RJ, Richards JP (eds) One Hundredth Anniversary Volume. Society of Economic Geologists, pp 299–336

Millonig LJ, Albert R, Gerdes A, Avigad D, Dietsch C (2020) Exploring laser ablation U–Pb dating of regional metamorphic garnet–the Straits Schist, Connecticut, USA. Earth Planet Sci Lett 552:116589

Neymark LA, Holm-Denoma CS, Moscati RJ (2018) In situ LA-ICPMS U–Pb dating of cassiterite without a known-age matrix-matched reference material: examples from worldwide tin deposits spanning the Proterozoic to the tertiary. Chem Geol 483:410–425

Ondrus P, Veselovsky F, Gabasova A, Hlousek J, Srein V (2003) Geology and hydrothermal vein system of the Jachymov (Joachimsthal) ore district. J Geosci 48:3–18

Papeschi S, Musumeci G, Mazzarini F (2017) Heterogeneous brittle-ductile deformation at shallow crustal levels under high thermal conditions: the case of a synkinematic contact aureole in the inner northern Apennines, southeastern Elba Island, Italy. Tectonophysics 717:547–564. https://doi.org/10.1016/j.tecto.2017.08.020

Peng Q, Bromley AV (1992) Fluid inclusion studies of the skarn-type tin mineralization at Red-A-ven, Northwest Dartmoor, England. Chin J Geochem 11:362–369. https://doi.org/10.1007/BF02869067

Raimbault L, Cuney M, Azencott C, Duthou J-L, Joron JL (1995) Geochemical evidence for a multistage magmatic genesis of Ta-Sn-Li mineralization in the granite at Beauvoir, French Massif Central. Econ Geol 90:548–576. https://doi.org/10.2113/gsecongeo.90.3.548

Reed MH (2006) Sulfide mineral precipitation from hydrothermal fluids. Rev Mineral Geochem 61:609–631

Reinhardt N, Frenzel M, Meinert LD, Gutzmer J, Kürschner T, Burisch M (2021) Mineralogy and fluid characteristics of the Waschleithe Zn skarn – a distal part of the Schwarzenberg mineral system, Erzgebirge Germany. Ore Geol Rev 131:104007. https://doi.org/10.1016/j.oregeorev.2021.104007

Reinhardt N, Gerdes A, Beranoaguirre A, Frenzel M, Meinert LD, Gutzmer J, Burisch M (2022) Timing of magmatic-hydrothermal activity in the Variscan orogenic belt: LA-ICP-MS U–Pb geochronology of skarn-related garnet from the Schwarzenberg District, Erzgebirge. Miner Deposita 57:1071–1087. https://doi.org/10.1007/s00126-021-01084-x

Roedder E (1984) Fluid inclusion. Rev Mineral 12:1–644

Romer RL, Kroner U (2015) Sediment and weathering control on the distribution of Paleozoic magmatic tin–tungsten mineralization. Miner Deposita 50:327–338. https://doi.org/10.1007/s00126-014-0540-5

Romer RL, Kroner U (2016) Phanerozoic tin and tungsten mineralization—tectonic controls on the distribution of enriched protoliths and heat sources for crustal melting. Gondwana Res 31:60–95. https://doi.org/10.1016/j.gr.2015.11.002

Romer RL, Thomas R, Stein HJ, Rhede D (2007) Dating multiply overprinted Sn-mineralized granites—examples from the Erzgebirge, Germany. Miner Deposita 42:337–359. https://doi.org/10.1007/s00126-006-0114-2

Rötzler K (1995) Die PT-Entwicklung der Metamorphite des Mittel- und Westerzgebirges. Scientific Technical Report 95/14. Geoforschungszentrum Potsdam

Schmädicke E, Mezger K, Cosca MA, Okrusch M (1995) Variscan Sm-Nd and Ar-Ar ages of eclogite facies rocks from the Erzgebirge, Bohemian Massif. J Metamorph Geol 13:537–552. https://doi.org/10.1111/j.1525-1314.1995.tb00241.x

Schmidt C (2018) Formation of hydrothermal tin deposits: Raman spectroscopic evidence for an important role of aqueous Sn(IV) species. Geochim Cosmochim Acta 220:499–511. https://doi.org/10.1016/j.gca.2017.10.011

Schuppan W, Hiller A (2012) Die Komplexlagerstätten Tellerhäuser und Hämmerlein: Uranbergbau und Zinnerkundung in der Grube Pöhla der SDAG Wismut. Bergbau in Sachsen, 17. Sächsisches Landesamt für Umwelt, Landwirtschaft und Geologie, Dresden

Seman S, Stockli DF, McLean NM (2017) U-Pb geochronology of grossular-andradite garnet. Chem Geol 460:106–116. https://doi.org/10.1016/j.chemgeo.2017.04.020

Simons B, Andersen JC, Shail RK, Jenner FE (2017) Fractionation of Li, Be, Ga, Nb, Ta, In, Sn, Sb, W and Bi in the peraluminous Early Permian Variscan granites of the Cornubian Batholith: Precursor processes to magmatic-hydrothermal mineralisation. Lithos 278-281:491–512. https://doi.org/10.1016/j.lithos.2017.02.007

Steele-MacInnis M, Bodnar RJ, Naden J (2011) Numerical model to determine the composition of H2O–NaCl–$CaCl_2$ fluid inclusions based on microthermometric and microanalytical data. Geochim Cosmochim Acta 75:21–40. https://doi.org/10.1016/j.gca.2010.10.002

Steele-MacInnis M, Lecumberri-Sanchez P, Bodnar RJ (2012) HokieFlincs_H_2O-NaCl: a Microsoft Excel spreadsheet for interpreting microthermometric data from fluid inclusions based on the PVTX properties of H_2O–NaCl. Comp Geosci 49:334–337. https://doi.org/10.1016/j.cageo.2012.01.022

Štemprok M (1967) Genetische Probleme der Zinn-Wolfram-Vererzung im Erzgebirge. Miner Deposita 2:102–118

Swinkels LJ, Schulz-Isenbeck J, Frenzel M, Gutzmer J, Burisch M (2021) Spatial and temporal evolution of the Freiberg epithermal Ag-Pb-Zn district, Germany. Econ Geol 116:1649–1667. https://doi.org/10.5382/econgeo.4833

Tapster J, Bright JWG (2020) High-precision ID-TIMS cassiterite U–Pb systematics using a low-contamination hydrothermal decomposition: implications for LA-ICP-MS and ore deposit geochronology. GChron 2:425–441

Taylor RG (1979) Geology of tin deposits. Elsevier, p 543

Tera F, Wasserburg GJ (1972) U-Th-Pb systematics in three Apollo 14 basalts and the problem of initial Pb in lunar rocks. Earth Planet Sci Lett 14:281–304. https://doi.org/10.1016/0012-821x(72)90128-8

Thomas R, Klemm W (1997) Microthermometric study of silicate melt inclusions in Variscan granites from SE Germany: volatile contents and entrapment conditions. J Petrol 38:1753–1765. https://doi.org/10.1093/petroj/38.12.1753

Tichomirowa M, Sergeev S, Berger H-J, Leonhardt D (2012) Inferring protoliths of high-grade metamorphic gneisses of the Erzgebirge using zirconology, geochemistry and comparison with lower-grade rocks from Lusatia (Saxothuringia, Germany). Contrib Mineral Petrol 164:375–396. https://doi.org/10.1007/s00410-012-0742-8

Tichomirowa M, Käßner A, Sperner B, Lapp M, Leonhardt D, Linnemann U, Münker C, Ovtcharova M, Pfänder JA, Schaltegger U, Sergeev S, von Quadt A, Whitehouse M (2019) Dating multiply overprinted granites: the effect of protracted magmatism and fluid flow on dating systems (zircon U-Pb: SHRIMP/SIMS, LA-ICP-MS, CA-ID-TIMS; and Rb–Sr, Ar–Ar) – granites from the Western Erzgebirge (Bohemian Massif, Germany). Chem Geol 519:11–38. https://doi.org/10.1016/j.chemgeo.2019.04.024

Tischendorf G, Förster H-J (1990) Acid magmatism and related metallogenesis in the Erzgebirge. Geol J 25:443–454. https://doi.org/10.1002/gj.3350250326

Tischendorf G, Wasternack J, Bolduan H, Bein E, Tischendorf G (1965) Zur Lage der Granitoberfläche im Erzgebirge und Vogtland mit Bemerkungen über ihre Bedeutung für die Verteilung der endogenen Lagerstätten. Z angew Geol 11(1965):410–423

von Seckendorff V, Timmerman MJ, Kramer W, Wrobel P (2004) New 40 Ar/39 Ar ages and geochemistry of late Carboniferous-early Permian lamprophyres and related volcanic rocks in the Saxothuringian Zone of the Variscan orogen (Germany). Geol Soc London Spec Publ 223:335–359. https://doi.org/10.1144/GSL.SP.2004.223.01.15

Warkus F (1997) U-Pb Altersdatierungen an Graniten des Erzgebirges und deren geochemische Einordnung (Unpubl Dipl thesis). University Göttingen, p 68

Willner AP, Rötzler K, Maresch WV (1997) Pressure-temperature and fluid evolution of quartzo-feldspathic metamorphic rocks with a relic high-pressure, granulite-facies history from the Central Erzgebirge (Saxony, Germany). J Petrol 1997:307–336

Zhang R, Lehmann B, Seltmann R, Sun W, Li C (2017) Cassiterite U-Pb geochronology constrains magmatic-hydrothermal evolution in complex evolved granite systems: the classic Erzgebirge tin province (Saxony and Bohemia). Geology 45:1095–1098. https://doi.org/10.1130/G39634.1